J. Fluid Mech. (1995), *vol.* 283, *pp.* 43–95

Dynamics of direct large–small scale couplings in coherently forced turbulence: concurrent physical- and Fourier-space views

By P. K. YEUNG†, JAMES G. BRASSEUR AND QUNZHEN WANG‡

Department of Mechanical Engineering, The Pennsylvania State University, University Park, PA 16802, USA

(Received 17 September 1991 and in revised form 30 July 1994)

As discussed in a recent paper by Brasseur & Wei (1994), scale interactions in fully developed turbulence are of two basic types in the Fourier-spectral view. The cascade of energy from large to small scales is embedded within 'local-to-non-local' triadic interactions separated in scale by a decade or less. 'Distant' triadic interactions between widely disparate scales transfer negligible energy between the largest and smallest scales, but directly modify the structure of the smallest scales in relationship to the structure of the energy-dominated large scales. Whereas cascading interactions tend to isotropize the small scales as energy moves through spectral shells from low to high wavenumbers, distant interactions redistribute energy within spectral shells in a manner that leads to anisotropic redistributions of small-scale energy and phase in response to anisotropic structure in the large scales. To study the role of long-range interactions in small-scale dynamics, Yeung & Brasseur (1991) carried out a numerical experiment in which the marginally distant triads were purposely stimulated through a coherent narrow-band anisotropic forcing at the large scales readily interpretable in both the Fourier- and physical-space views. It was found that, after one eddy turnover time, the smallest scales rapidly became anisotropic as a direct consequence of the marginally distant triadic group in a manner consistent with the distant triadic equations. Because these asymptotic equations apply in the infinite Reynolds number limit, Yeung & Brasseur argued that the observed long-range effects should be applicable also at high Reynolds numbers.

We continue the analysis of forced simulations in this study, focusing (i) on the detailed three-dimensional restructuring of the small scales as predicted by the asymptotic triadic equations, and (ii) on the relationship between Fourier- and physical-space evolution during forcing. We show that the three-dimensional restructuring of small-scale energy and vorticity in Fourier space from large-scale forcing is predicted in some detail by the distant triadic equations. We find that during forcing the distant interactions alter small-scale structure in two ways: energy is redistributed anisotropically within high-wavenumber spectral shells, and phase correlations are established at the small scales by the distant interactions. In the numerical experiments, the long-range interactions create two pairs of localized volumes of concentrated energy in three-dimensional Fourier space at high wavenumbers in which the Fourier modes are phase coupled. Each pair of locally phase-correlated volumes of Fourier modes separately corresponds to aligned vortex

† Current address: School of Aerospace Engineering, Georgia Institute of Technology, Atlanta, GA 30332, USA.

‡ Current address: Department of Mechanical Engineering, University of Vermont, Burlington, VT 05405, USA.

tubes in physical space in two orthogonal directions. We show that the dynamics of distant interactions in creating small-scale anisotropy may be described in physical space by differential advection and distortion of small-scale vorticity by the coherent large-scale energy-containing eddies, producing anisotropic alignment of small-scale vortex tubes.

Scaling arguments indicate a disparity in timescale between distant triadic interactions and energy-cascading local-to-non-local interactions which increases with scale separation. Consequently, the small scales respond to forcing initially through the distant interactions. However, as energy cascades from the large-scale to the small-scale Fourier modes, the stimulated distant interactions become embedded within a sea of local-to-non-local energy cascading interactions which reduce (but do not eliminate) small-scale anisotropy at later times. We find that whereas the small-scale structure is still anisotropic at these later times, the second-order velocity moment tensor is insensitive to this anisotropy. Third-order moments, on the other hand, do detect the anisotropy. We conclude that whereas a single statistical measure of anisotropy can be used to indicate the presence of anisotropy, a null result in that measure does not necessarily imply that the signal is isotropic. The results indicate that non-equilibrium non-stationary turbulence is particularly sensitive to long-range interactions and deviations from local isotropy.

1. Introduction: large–small scale couplings at large Reynolds numbers and isotropy in the small scales

In fully developed turbulent flows, inertial nonlinearities create and maintain motions over a wide range of lengthscales. The motivation behind the current study is to develop a more complete understanding of interscale dynamics in general, and the dynamics underlying large–small scale interactions in high Reynolds number turbulence in particular, in context with hypotheses introduced by Kolmogorov in (1941).

Kolmogorov (1941) hypothesized that, at sufficiently high outer-scale Reynolds numbers, the distribution of velocity differences δu at scale r (*a*) is statistically isotropic and (*b*) depends only on the local lengthscale r, dissipation rate ϵ and kinematic viscosity ν if r is much smaller than the outer scale l. Kolmogorov further hypothesized that within an inertia-dominated subset of scales r much larger than the viscous scale η (but still much smaller than l), the distribution of δu is independent of ν, implying no direct frictional effects at these scales. Upon these simple hypotheses Kolmogorov formulated a similarity theory which remains a strong influence on turbulence theory, analysis, measurement and modelling. Whereas Kolmogorov formulated his similarity theory for stationary high Reynolds number turbulence in equilibrium at all scales, the hypotheses underlying the theory are often applied more broadly.

Kolmogorov's hypotheses have far-reaching kinematic and dynamic implications which continue to be explored in the literature. For example, for there to be no influence of the outer energy-dominated scales on the inner dissipation-dominated scales at large scale separations (i.e. high Reynolds numbers), no direct energy transfer can take place between these disparate scales. This, in turn, implies that energy must travel, on average, from the large-scale motions l to the small-scale motions η within 'local' scale interactions (Onsager 1949) through an inertia-dominated range of intermediate scales with negligible dissipation. The rate of dissipation should therefore scale on large-scale velocity and time scales in equilibrium turbulence (Kolmogorov

1941). Grid turbulence data support this conclusion for Taylor microscale Reynolds numbers R_λ above roughly 50 (Batchelor 1953; Sreenivasan 1985; where R_λ is defined with component r.m.s. and longitudinal microscale).

Whereas Kolmogorov did not elaborate on the dynamical implications of his 1941 similarity theory, many others have. Brasseur & Corrsin (1987), for example, showed that Navier–Stokes dynamics implies the absence of direct energy transfer between asymptotically disparate scales of motion, consistent with the Kolmogorov hypothesis of statistically local energy transfer at scales far removed from the outer scale. The analysis of Brasseur & Wei (1994) indicates that, within the triadic dynamics of the Navier–Stokes equation, the separation between disparate scales must be greater than roughly 15 for negligible energy transfer to exist between those disparate scales.

The absence of direct energy transfer between disparate scales, however, is dynamically insufficient to argue for the absence of all influence of the energy-containing scales l on scales $r \ll l$. Batchelor (1953), for example, noted that the hypothesis of local isotropy at scales $r \ll l$ implies statistical independence between motions at scale l and motions at scales r, which itself implies a dynamical decoupling of the smallest scales of motion from the largest scales at asymptotically large Reynolds numbers. The notion is that, the greater the disparity between 'small' scales and large-scale energy-containing motions, the more dynamically independent are the small-scale motions from the large-scale motions, in an ensemble average sense. Because the ratio of integral scale l and Taylor microscale λ to Kolmogorov scale η scales as $l/\eta \sim R_\lambda^{3/2}$ and $\lambda/\eta \sim R_\lambda$ in equilibrium turbulence, the disparity between large scales and small scales becomes asymptotically large at asymptotically high Reynolds numbers (in equilibrium turbulence). The conjecture of large–small scale independence is therefore an asymptotic argument which theoretically improves in the limits of smallest dynamical scale ($r \to \eta$) at fixed Reynolds number, and asymptotically increasing Reynolds number at fixed small-scale lengthscale (relative to λ or η, say). If the conjecture of large-scale/small-scale independence is correct, then external information embedded in the large scales can only be transmitted to the small scales via multiple localized cascading interactions, through which, it is argued, memory of large-scale structure is lost at the smallest scales. At large scale separations, then, the smallest scales would attain a directionally independent, or 'locally' isotropic state, where 'local' refers to scales of motion r much smaller than the outer externally forced scales. Because local isotropy depends both on independence between large and small scales and on multiple cascading interactions, the argument is an asymptotic one which improves with decreasing scale ($r \to \eta$) at fixed R_λ, and increasing Reynolds number ($R_\lambda \to \infty$).

Whereas the hypothesis of no direct energy transfer between the large and small scales has good experimental support (above), the hypothesis of local isotropy remains controversial. The issue has been studied experimentally (Antonia, Anselmet & Chambers 1986; Browne, Antonia & Shah 1987; Champagne 1978; George & Hussein 1991; Karyakin, Kuznetsov & Praskovsky 1991; Saddoughi & Veeravalli 1994), numerically (Yeung & Brasseur 1991; Kim & Antonia 1993; Brasseur & Wei 1994) and theoretically (Brasseur 1991; Durbin & Speziale 1991; Yeung & Brasseur 1991; Lumley 1992; Nelkin 1993). Useful overviews of experimental issues are given by Sreenivasan (1991) and Van Atta (1991). Triad-based spectral arguments are summarized by Brasseur & Wei (1994).

The motivation behind the current study is to develop a more complete understanding of the dynamics underlying large–small scale interactions in high Reynolds number turbulence and the widely applied hypotheses of large–small scale

independence and local isotropy, *concurrently in the Fourier-space and physical-space views*. This study is a continuation of the analysis by Yeung & Brasseur (1991, hereafter referred to as YB), which itself is based on the controversial arguments of Brasseur (1991). Brasseur observed that, because the nonlinear terms in the Navier–Stokes equation written in Fourier space contain explicit interactions between disparate scales which retain a zeroth-order contribution in the limit of infinite scale separation, the small scales are not, in principle, independent of the large scales at infinite Reynolds numbers. Furthermore, although it was shown that no energy is transferred directly between the large and small scales in these triadic interactions (Brasseur & Corrsin 1987), the large scales directly influence small scale evolution. The structure of the distant triadic terms in such that large-scale anisotropy, in principle, forces anisotropic energy exchange among the small scale modes. Given sufficient time, then, the distant triadic interactions in principle produce anisotropic motions at the small scales. The level of anisotropy induced at the small scales depends on the net effect of all distant interactions which must complete with other dynamical effects, principally the isotropizing effects of local and nonlocal triadic interactions (Brasseur 1991; Brasseur & Yeung 1991; Brasseur & Wei 1994). Which effects dominate at any point in time depends on a number of factors, including separation between scales, strength and temporal coherence of large-scale anisotropy, and previous history.

In the numerical experiment of YB, four large-scale Fourier modes were coherently forced in a highly anisotropic manner in order to stimulate marginally distant triadic interactions within the smallest dynamical scales of initially isotropic turbulence at a moderate Reynolds number. It was found that the smallest scales became anisotropic after one eddy turnover time and, consistent with the form of the distant triadic equations, the smallest scales develop the highest level of anisotropy. The study showed that anisotropic small-scale energy transfer was a direct consequence of the marginally distant triadic interactions, suggesting that the effect should exist also at high Reynolds numbers. However, the structure of the anisotropic small-scale turbulence, the manner in which anisotropic small-scale structure is induced by large-scale forcing, and the corresponding interpretation of the distant interactions in physical space, were not discussed. These issues are addressed in the current study.

We find, in this study, that the form of the distant triadic equations, which apply in the asymptotic limit of infinite Reynolds number, explain most of the details of small-scale restructuring in Fourier space, and that the small-scale restructuring is of two types: redistribution of energy within high-wavenumber shells, and a restructuring of the phase relationships among small-scale Fourier modes. We show that the physical space description of direct small-scale restructuring due to large-scale forcing is advection and distortion of small-scale vortical elements by energy-dominated eddies. Very interesting is the observation that localized regions in Fourier space at high wavenumbers directly describe subsets of aligned vortex tubes in physical space.

The competition between distant and local-to-nonlocal triadic interactions becomes evident in the return towards isotropy of the small scales after continued large-scale forcing, indicating that non-equilibrium non-stationary turbulence is particularly sensitive to direct large–small scale interactions and deviations from local isotropy. We show that this return to isotropy is related to the ratio of energy in the large scales to the small scales, which itself is related to the relative importance of distant to local and nonlocal interactions. Very important is the observation that, while anisotropy in the second moment returns to zero at the small scales, the structure of the turbulence is still anisotropic. Third-order moments, however, do capture this anisotropy, indicating that definitive tests of local isotropy cannot be made with single anisotropy measures.

2. Triadic arguments underlying the current study

Analytically, scale interactions are conveniently analysed using Fourier decomposition, where a scale of motion is characterized as a Fourier mode $\boldsymbol{k} = k\hat{\boldsymbol{e}}_k$, with lengthscale $r \sim k^{-1}$, direction $\hat{\boldsymbol{e}}_k$, energy $e(\boldsymbol{k}) = \hat{\boldsymbol{u}}(\boldsymbol{k})\cdot\hat{\boldsymbol{u}}^*(\boldsymbol{k})$, and phase (the real and imaginary parts of $\hat{\boldsymbol{u}}$):

$$\boldsymbol{u}(\boldsymbol{x}, t) = \sum_{\boldsymbol{k}} \hat{\boldsymbol{u}}(\boldsymbol{k}, t)\, \mathrm{e}^{\mathrm{i}\boldsymbol{k}\cdot\boldsymbol{x}}. \tag{1}$$

The evolution of Fourier mode $\boldsymbol{k}$ in Navier–Stokes dynamics is given by

$$[\dot{\hat{\boldsymbol{u}}}(\boldsymbol{k})]_{NL} \equiv \left[\frac{\partial}{\partial t} + \nu k^2\right]\hat{\boldsymbol{u}}(\boldsymbol{k}) = -\mathrm{i}\sum_{\boldsymbol{p}} \hat{\boldsymbol{u}}(\boldsymbol{p})_{\perp\boldsymbol{k}}[\boldsymbol{k}\cdot\hat{\boldsymbol{u}}(\boldsymbol{k}-\boldsymbol{p})], \tag{2}$$

where NL refers to the nonlinear terms and

$$\hat{\boldsymbol{u}}(\boldsymbol{p})_{\perp\boldsymbol{k}} = [\boldsymbol{I} - \boldsymbol{k}\boldsymbol{k}/k^2]\cdot\hat{\boldsymbol{u}}(\boldsymbol{p})$$

is the vectorial projection of $\hat{\boldsymbol{u}}(\boldsymbol{p})$ onto a plane perpendicular to $\boldsymbol{k}$, $\boldsymbol{I}$ being the identity tensor. The rate of energy change in mode $\boldsymbol{k}$ is given by

$$[\dot{e}(\boldsymbol{k})]_{NL} = \left[\frac{\partial}{\partial t} + 2\nu k^2\right]e(\boldsymbol{k}) = 2\,\mathrm{Im}\left\{\sum_{\boldsymbol{p}} \hat{\boldsymbol{u}}^*(\boldsymbol{k})\cdot\hat{\boldsymbol{u}}(\boldsymbol{p})[\boldsymbol{k}\cdot\hat{\boldsymbol{u}}(\boldsymbol{k}-\boldsymbol{p})]\right\}, \tag{3}$$

where * denotes complex conjugate. The nonlinear intermodal interactions in Newton's law are contained within a sum over all triads of Fourier modes containing $\boldsymbol{k}$. Each triad is formed by a triangle of wave vectors, $\boldsymbol{k}$, $\boldsymbol{p}$ and $\boldsymbol{q} = \boldsymbol{k}-\boldsymbol{p}$ and each wave vector $\boldsymbol{k}$ has a negative counterpart, $-\boldsymbol{k}$ such that $\hat{\boldsymbol{u}}(-\boldsymbol{k}) = [\hat{\boldsymbol{u}}(\boldsymbol{k})]^*$ and $\dot{e}(-\boldsymbol{k}) = \dot{e}(\boldsymbol{k})$.

It was pointed out by Brasseur (1991) that the direct influence of large-scale structure on small-scale dynamics is given by the net effect of all 'distant' triadic interactions in which $\boldsymbol{k}$ is in the small scales and $\boldsymbol{p}$ is within the energy-containing scales. That is, the nonlinear effects of the energy-dominated, or 'large scales', on the small scales is given by the first term in the following restructuring of equations (1) and (2):

$$\begin{aligned}[\dot{\boldsymbol{u}}(\boldsymbol{x}, t)]_{\substack{small\\scales}} &= \sum_{\substack{\boldsymbol{k}\in\\small\ scales}} \{[\dot{\hat{\boldsymbol{u}}}(\boldsymbol{k})]_{NL}\}\, \mathrm{e}^{\mathrm{i}\boldsymbol{k}\cdot\boldsymbol{x}} \\ &= \sum_{\substack{\boldsymbol{k}\in\\small\\scales}} \left\{ \sum_{\substack{\boldsymbol{p}\in\\large\\scales}} [\text{distant triadic interactions, } p/k \ll 1] + \sum_{\substack{\boldsymbol{p}\in\\other\\scales}} [\text{all other triads}] \right\} \mathrm{e}^{\mathrm{i}\boldsymbol{k}\cdot\boldsymbol{x}}. \end{aligned} \tag{4}$$

Collections of Fourier modes within high-wavenumber shells describe the motions with 'small-scale' structures in physical space (see Brasseur & Wang 1992). The hypotheses of large–small scale independence and local isotropy imply that the cumulative effects of the first group on the right-hand side of (4) disappears in the asymptotic limit of infinite scale separation, $k/p \sim q/p \to \infty$ (implying infinite Reynolds numbers). Brasseur (1991) argued that if an arbitrary member of the 'distant' triadic group does not disappear in the limit $k/p \sim q/p \to \infty$, then the group as a whole does not disappear at infinite Reynolds numbers, in principle, and that small-scale evolution contains some level of large-scale dependence. The general characteristics of a single arbitrary distant triadic interaction, then, would be reflected in the general characteristics of the ensemble of distant interactions, and therefore the general characteristics of the first group in (4).

Brasseur & Corrsin (1987) isolated an arbitrary distant triadic interaction in the asymptotic limit $\delta \equiv p/k \sim p/q \to 0$ and found a zeroth-order contribution, implying that the first term in (4) does not asymptotically disappear in the high Reynolds number limit:

$$\left.\begin{aligned} [\dot{\hat{\boldsymbol{u}}}(\boldsymbol{p})]_{NL} &= O(\delta), \\ [\dot{\hat{\boldsymbol{u}}}(\boldsymbol{k})]_{NL} &= -\mathrm{i}\{\hat{\boldsymbol{u}}(\boldsymbol{q})[\boldsymbol{k}\cdot\hat{\boldsymbol{u}}(\boldsymbol{p})]\} + O(\delta), \\ [\dot{\hat{\boldsymbol{u}}}(\boldsymbol{q})]_{NL} &= -\mathrm{i}\{\hat{\boldsymbol{u}}(\boldsymbol{k})[\boldsymbol{k}\cdot\hat{\boldsymbol{u}}(\boldsymbol{p})]\} + O(\delta), \end{aligned}\right\} \tag{5}$$

where $\boldsymbol{q} = \boldsymbol{k} - \boldsymbol{p}$. The corresponding equations for energy exchange within an arbitrary distant interaction are

$$\left.\begin{aligned} [\dot{e}(\boldsymbol{p})]_{NL} &= O(\delta), \\ [\dot{e}(\boldsymbol{k})]_{NL} = -[\dot{e}(\boldsymbol{q})]_{NL} &= 2\,\mathrm{Im}\{\hat{\boldsymbol{u}}^*(\boldsymbol{k})\cdot\hat{\boldsymbol{u}}(\boldsymbol{q})[\boldsymbol{k}\cdot\hat{\boldsymbol{u}}(\boldsymbol{p})]\} + O(\delta). \end{aligned}\right\} \tag{6}$$

We define a 'distant' triadic interaction between disparate modes (where small-scale mode energy is of order or less than large-scale mode energy) as one which satisfies (5) and (6) is a very good approximation. This asymptotic form implies that no direct energy transfer takes place between the large and small scales in the limit $\delta \to 0$, consistent with Kolmogorov (1941). However, whereas (5) and (6) imply that the small scales have no influence on the large scales in the asymptotic limit, large-scale structure directly modulates the evolutions of small-scale Fourier modes through the coupling terms involving the large-scale modes, $\hat{\boldsymbol{u}}(\boldsymbol{p})$. Furthermore, as was argued by Brasseur (1991), the structure of the coupling term is such to imply anisotropic energy exchange at the small scales within the distant triadic group if the large scales are anisotropic.

It has been argued by Waleffe (1992) that whereas individual triadic interactions may not disappear in the asymptotic limit, it is possible that the individual energy transfers within members of the distant triadic group in equation (4) cancel, leaving no net effect of this group. In the forced simulation here and in YB this is not the case, and is therefore not true as a general statement. Furthermore, in context with local isotropy, it is important to recognize the distinction between net *energy transfer* at the small scales within the distant triadic group

$$\begin{aligned} T_{small\ scales} &\equiv \sum_{\substack{\boldsymbol{k}\in \\ small\ scales}} [\dot{e}(\boldsymbol{k})]_{NL} \\ &= \sum_{\substack{\boldsymbol{k}\in \\ small \\ scales}} \left\{ \sum_{\substack{\boldsymbol{p}\in \\ large \\ scales}} [\text{triadic interactions where } p/k \ll 1] + \sum_{\substack{\boldsymbol{p}\in \\ other \\ scales}} [\text{all other triads}] \right\}, \end{aligned} \tag{7}$$

and *structural evolution* of three-dimensional physical space relative to three-dimensional Fourier space, as described by equation (4). Structural evolution in physical space involves a redistribution of energy and/or phase relationships among Fourier modes in Fourier space. As demonstrated in YB, the distant triadic group allows large-scale structure to directly alter small-scale structure without altering the energy content within the small scales. Brasseur & Wei (1994) point out that the importance of the distant triadic group in (4) in small-scale dynamics centres on the relative contribution of the distant triadic group to (4) in comparison with all other dynamical effects. Whereas the relative importance of the distant group may be minimal, for example, in the inertial subrange in stationary high Reynolds number turbulence, the effect of the distant group may be very important, even dominant, in non-stationary non-equilibrium turbulence for certain periods of time.

Furthermore, Brasseur (1991) points out that the relative contribution of individual

distant triadic interactions in the first group in (4) to roughly local triads is given in the asymptotic limit by

$$\frac{[\dot{e}(k_{SS})]_{distant}}{[\dot{e}(k_{SS})]_{local/non\text{-}local}} \sim \left(\frac{E(k_{LS})}{E(k_{SS})}\right)^{1/2} \frac{k_{SS}}{k_{LS}}, \tag{8}$$

where $E(k_{LS}) \sim e(k_{LS})\, k_{LS}^2$ is the peak in the energy spectrum (LS denotes large scale) and $E(k_{SS}) \sim e(k_{SS})\, k_{SS}^2$ is the spectral energy in a high-wavenumber shell centred on k_{SS} (SS denotes small scales). Thus, the relative importance of distant interactions in small-scale dynamics increases asymptotically with decreasing scale, suggesting that distant interactions become progressively more important within progressively smaller scales (shown in Brasseur & Wei 1994). Consequently, the effects of the distant group should be sought in the limit of decreasing scale for fixed Reynolds number as well as for progressively higher Reynolds numbers.

If deviations from local isotropy arise from the distant triadic group due to large-scale restructuring, the triadic equations suggest that deviations should be greater in the smallest scales (§3.1) and should appear initially at the smallest scales (§3.4). This conclusion is opposite to the traditional view that large–small scale coupling weakens with decreasing scale, and it is upon these observations that the current study and that of YB are based.

3. The numerical experiment: predictions in the asymptotic limit

The numerical experiment of YB was designed to coherently stimulate well-defined distant interactions in a manner which can be understood concurrently in physical space and in Fourier space. Based on the specific structure of the forcing, a number of predictions follow from the distant triadic equations (6) which are relevant only to the distant triadic group in equation (4) and not predictable by the local and non-local triadic groups. We argue that if the numerical simulations display dynamics at the smallest resolved scales which follow only from the distant triadic group, then the observed characteristic is a general effect of direct interaction between large and small scales which applies at infinite scale separations, and therefore at large Reynolds numbers. As computer speed and memory increase, this argument must be tested at continually greater scale separations.

In the earlier work of YB the development of anisotropy at high wavenumbers in Fourier space due to coherent anisotropic forcing in four low-wavenumber modes was shown to be a direct consequence of the distant triadic group. The small-scale anisotropy increased with increasing wavenumber consistent with the distant form of the triadic equations, (5) and (6), which indicate that the effect of distant triadic interactions increases relative to local interactions with increasing wavenumber at the smallest dynamically relevant scales (Brasseur 1991). In the current paper we study the details of small-scale restructuring in three-dimensional Fourier space and physical space concurrently. A number of predictions are made here which follow only from the asymptotic form relevant to distant triadic interactions. These predictions are shown in following sections to be consistent with the simulations.

3.1. *Redistribution of small-scale energy by forcing*

Consider the manner in which mode energy is rearranged within high-wavenumber shells by the distant group of triadic interactions in comparison with the local and non-local groups in high Reynolds number fully developed turbulence (Brasseur & Yeung 1991). We begin with statistically isotropic turbulence at high Reynolds numbers. As

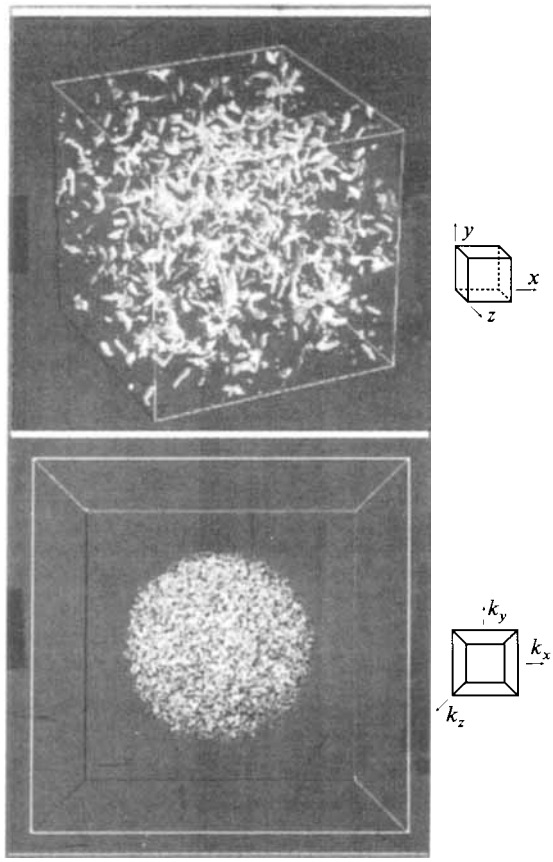

FIGURE 1. Three-dimensional isosurfaces of the enstrophy (*a*) in physical space and (*b*) in Fourier space for isotropic turbulence just before forcing. The isosurface levels of $\omega_i(\boldsymbol{x})\,\hat{\omega}_i(\boldsymbol{x})$ in (*a*) and $\hat{\omega}_i(\boldsymbol{k})\,\hat{\omega}_i^*(\boldsymbol{k})$ in (*b*) are 2.5 and 0.001 r.m.s. above the mean value of the enstrophy field, respectively. Note that statistical isotropy in physical space implies spherical symmetry in Fourier space.

illustrated in figure 1, isosurfaces of constant energy (or enstrophy) in isotropic turbulence are spheres centred at the origin in $\boldsymbol{k}$-space, the radius of the sphere being inversely proportional to the scale of turbulence. Now imagine anisotropic forcing at the large scales such that the four low-wavenumber modes shown in figure 2, $\pm\boldsymbol{k}_F^{(1)}$ and $\pm\boldsymbol{k}_F^{(2)}$, rapidly increase in energy relative to all other Fourier modes (details are given in §4). The four modes are forced coherently through the Fourier coefficients $\hat{\boldsymbol{u}}(\boldsymbol{k}_F)$ which are within the (k_x, k_y)-plane. (This forcing corresponds, in physical space, to the addition of energy in an array of 16 counter-rotating vortices as shown in figure 3.) We ask, how will interscale transfer at the small scales be modified by this forcing and what spectral energy distribution will result?

Consider intermodal energy transfer $\dot{e}(\boldsymbol{k})$ among high-wavenumber modes $\boldsymbol{k}$ in response to this forcing. In particular, compare the response at the small scales to forcing within the distant triadic group, given by (6), with members from the local and non-local groups, given for triad $\boldsymbol{k}-\boldsymbol{p}-\boldsymbol{q}=0$ from (3) by

$$[\dot{e}(\boldsymbol{k})]_{NL} = 2\,\mathrm{Im}\{\hat{\boldsymbol{u}}^*(\boldsymbol{k})\cdot\hat{\boldsymbol{u}}(\boldsymbol{q})[\boldsymbol{k}\cdot\hat{\boldsymbol{u}}(\boldsymbol{p})]+\hat{\boldsymbol{u}}^*(\boldsymbol{k})\cdot\hat{\boldsymbol{u}}(\boldsymbol{p})[\boldsymbol{k}\cdot\hat{\boldsymbol{u}}(\boldsymbol{q})]\}. \tag{9}$$

Note in comparison with (6) that the second term in (9) is negligible when k/p is large. Consequently, when distant triadic interactions dominate (equation (8)), some

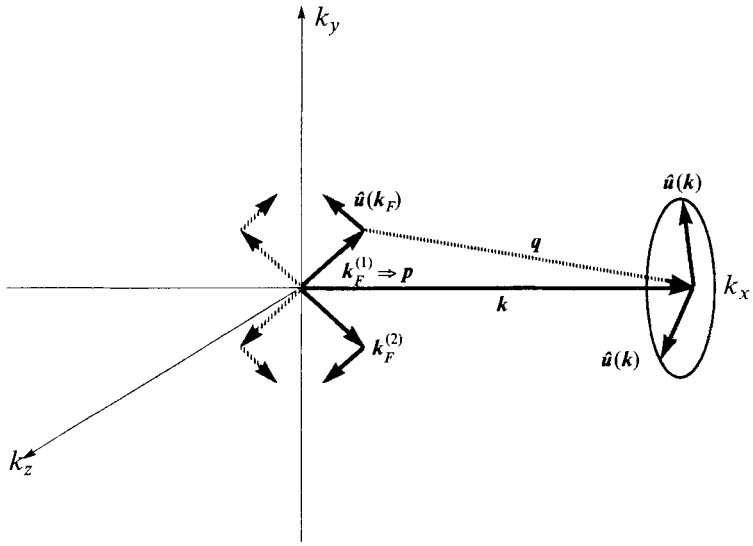

FIGURE 2. Schematic of forcing in Fourier space. The four forced large-scale Fourier modes and their Fourier coefficients are shown. These two pairs of modes are of equal magnitude and oriented at $\pm 45°$ and $\pm 135°$ to the positive k_x-axis in the (k_x, k_y)-plane. The real parts of the Fourier coefficients are zero and the imaginary parts are shown in the figure. Also illustrated is a single triadic interaction between a forced mode $\boldsymbol{k}_F$ and a high-wavenumber mode k (not drawn to scale).

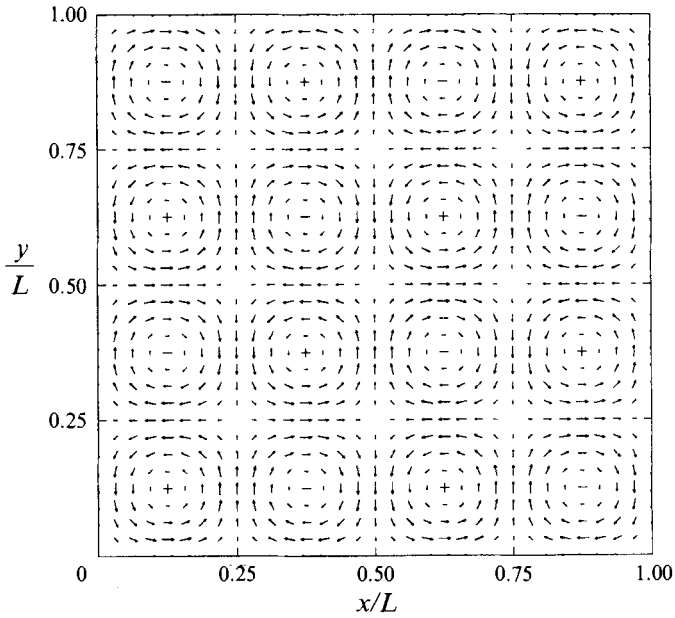

FIGURE 3. The forced velocity field in physical space. Shown are velocity vectors of the two-dimensional velocity field of the 16 large-scale counter-rotating (+ and −) vortices through which the initially isotropic turbulence is coherently forced. Coordinates are shown normalized by the length $L = 2\pi$ of the cubic solution domain. Note that stagnation points eventually form at locations in the (x, y)-plane equidistant from sets of four vortex cores.

differences in energy exchange at high wavenumbers may be anticipated, owing to the structure of the triadic equations particular to distant interactions.

Consider all triadic interactions within a high-wavenumber shell shortly after forcing, at a time when the only anisotropy within the turbulence comes from the four forced modes, $\pm\boldsymbol{k}_F^{(n)}$, $n = 1, 2$. Now identify $\boldsymbol{p}$ with one of the forced modes, $\boldsymbol{p} \equiv \boldsymbol{k}_F^{(1)}$, (refer to figure 2), and let $\boldsymbol{k}$ be an arbitrary mode within a high-wavenumber shell. Consider modal energy exchange $\dot{e}(\boldsymbol{k})$ with different triadic groups as a function of position within a high-wavenumber shell:

$$[\dot{e}(\boldsymbol{k})]_{NL} = [\dot{e}(\boldsymbol{k})]_{distant} + [\dot{e}(\boldsymbol{k})]_{other}, \tag{10}$$

where $[\dot{e}(\boldsymbol{k})]_{distant}$ is to be interpreted as all distant interactions between the forced mode $\boldsymbol{k}_F^{(1)}$ and modes $\boldsymbol{k}$ within a high-wavenumber shell. Consider, in particular, energy exchange within different members of $[\dot{e}(\boldsymbol{k})]_{distant}$, given by (6) in comparison with a local-to-non-local member of $[\dot{e}(\boldsymbol{k})]_{other}$, as predicted by (9). Because continuity forces wavevector $\boldsymbol{k}$ to be perpendicular to its Fourier coefficient $\hat{\boldsymbol{u}}(\boldsymbol{k})$, the dot products in (9) and (6) are zero when $\boldsymbol{k}$, $\boldsymbol{p}$ (and therefore $\boldsymbol{q}$) are parallel. Thus, $\dot{e}(\boldsymbol{k}) \approx 0$ within all triadic interactions among $\boldsymbol{k}_F^{(1)}$ and those high-wavenumber modes $\boldsymbol{k}$ which are nearly parallel to $\boldsymbol{k}_F^{(1)}$. The triadic equations therefore indicate that the contribution to $\dot{e}(\boldsymbol{k})$ in high-wavenumber modes $\boldsymbol{k}$ from distant interactions with $\boldsymbol{k}_F^{(1)}$ will be reduced when $\boldsymbol{k}$ is in a cone surrounding $\boldsymbol{k}_F^{(1)}$ relative to $\boldsymbol{k}$ outside the cone. Because $\boldsymbol{k}_F^{(1)}$ contains more energy than surrounding low-wavenumber modes, we conclude that non-isotropic forcing through $\boldsymbol{k}_F^{(1)}$ leads to non-isotropic energy exchange in high-wavenumber shells within the distant triadic group of (10).

More can be predicted from the distant triadic equations which are relevant only to the distant triadic group. Equation (5) indicates that only the first term in (9) is non-negligible within individual distant triadic interactions at large scale separation, the term that contains the combination, $\boldsymbol{k}\cdot\hat{\boldsymbol{u}}(\boldsymbol{p})$, where $\boldsymbol{p} = \boldsymbol{k}_F^{(1)}$. Because the modes $\pm\boldsymbol{k}_F^{(n)}$ are forced so that $\hat{\boldsymbol{u}}(\boldsymbol{k}_F)$ are confined to the (k_x, k_y)-plane, $\boldsymbol{k}\cdot\hat{\boldsymbol{u}}(\boldsymbol{p}) = 0$ for all high-wavenumber $\boldsymbol{k}$ in the z-direction, and $\dot{e}(\boldsymbol{k})$ is small in a cone surrounding the z-axis. This prediction is relevant only at large wavenumbers where the asymptotic form of the triadic equations are valid.

We conclude that $[\dot{e}(\boldsymbol{k})]_{distant}$ at high wavenumbers has a non-uniform distribution so as to be reduced within cones in the directions $\pm\boldsymbol{k}_F^{(n)}$, and in the direction $\hat{\boldsymbol{e}}_z$. Conversely, $[\dot{e}(\boldsymbol{k})]_{distant}$ is maximal along the k_x- and k_y-axes. Thus, within the distant triadic group, high-wavenumber modes surrounding the k_x and k_y axes are rapidly exchanging energy while those modes surrounding $\pm\boldsymbol{k}_F^{(n)}$ and the k_z axis are not. The cascade of energy from larger to small scales is dominantly within local and non-local triadic interactions (Brasseur & Wei 1994; Zhou 1993*a*, *b*), while the distant group tends to transfer energy laterally within high-wavenumber spectral shells (i.e. perpendicularly to high-wavenumber wavevectors) rather than from one shell to the next (Brasseur & Wei 1994). During forcing, $[\dot{e}(\boldsymbol{k})]_{distant}$ moves energy laterally within shells most rapidly among those modes surrounding the k_x- and k_y-axes, the distant interactions dominating interscale energy transfer in those regions. By contrast, in the high-wavenumber regions aligned with $\pm\boldsymbol{k}_F^{(n)}$ and $\hat{\boldsymbol{e}}_z$, $[\dot{e}(\boldsymbol{k})]_{distant}$ is suppressed and the transfer of energy to higher wavenumbers within local and non-local triadic interactions is relatively unimpeded by the distant triadic group, and energy is transported away from these regions to higher wavenumbers where it is more readily dissipated.

Prediction. Therefore, we predict that, over time, forcing through $\pm\boldsymbol{k}_F^{(n)}$ will lead to a redistribution of energy in high-wavenumber shells as a consequence of distant

interactions without direct energy transfer between the forced modes and the small scales. Specifically, forcing will cause a depletion of energy in the directions $\pm \boldsymbol{k}_F^{(n)}$ and $\hat{\boldsymbol{e}}_k$ relative to modes lying near the k_x- and k_y-axes as a consequence of the distant triadic group. The discussion surrounding (8) indicates that this redistribution of energy and consequent anisotropy will be *stronger at smaller scales.*

We show in §7 that the numerical simulations confirm this prediction and, because the characteristics of the distant triadic group are given in the limit of asymptotically large scale separations, we argue that the predicted characteristic would also exist at asymptotically high Reynolds numbers.

3.2. *Redistribution of small-scale phase by forcing*

Consider now the evolution of the Fourier coefficients within the high-wavenumber regions surrounding the k_x- and k_y-axes which, we argue, will contain most of the small-scale energy after forcing. As indicated by (4), the evolution of the velocity field at the small scales is given by the cumulative evolution of $[\dot{\hat{\boldsymbol{u}}}(\boldsymbol{k})]_{distant}$ and $[\dot{\hat{\boldsymbol{u}}}(\boldsymbol{k})]_{other}$ for all high-wavenumber $\boldsymbol{k}$, where 'distant' again implies interactions between modes $\boldsymbol{k}$ and the forced modes $\boldsymbol{p} \equiv \pm \boldsymbol{k}_F^{(n)}$, as given by (5). The corresponding evolution of $\boldsymbol{k}$ for an arbitrary member of the local or non-local groups is given from (2) by

$$[\dot{\hat{\boldsymbol{u}}}(\boldsymbol{k})]_{NL} = -\mathrm{i}\{\hat{\boldsymbol{u}}(\boldsymbol{q})_{\perp k}[\boldsymbol{k}\cdot\hat{\boldsymbol{u}}(\boldsymbol{p})] + \hat{\boldsymbol{u}}(\boldsymbol{p})_{\perp k}[\boldsymbol{k}\cdot\hat{\boldsymbol{u}}(\boldsymbol{q})]\}. \tag{11}$$

Comparing with (5) shows that when $p \ll k \sim q$, the second term in (11) is negligible and $\hat{\boldsymbol{u}}(\boldsymbol{q})_{\perp k} \to \hat{\boldsymbol{u}}(\boldsymbol{q})$. Consequently, whereas in local and non-local triadic interactions the direction of $[\dot{\hat{\boldsymbol{u}}}(\boldsymbol{k})]_{NL}$ varies greatly from interaction to interaction, in distant interactions $[\dot{\hat{\boldsymbol{u}}}(\boldsymbol{k})]_{NL} \propto \hat{\boldsymbol{u}}(\boldsymbol{q})$ and $[\dot{\hat{\boldsymbol{u}}}(\boldsymbol{q})]_{NL} \propto \hat{\boldsymbol{u}}(\boldsymbol{k})$, where $\boldsymbol{k}$ and $\boldsymbol{q}$ are the two high-wavenumber modes in the distant interaction. In other words, distant interactions tend, over time, to vectorially align the real and imaginary parts of the Fourier coefficients. Furthermore, the dot produced $\hat{\boldsymbol{u}}^*(\boldsymbol{k})\cdot\hat{\boldsymbol{u}}(\boldsymbol{q})$ in $[\dot{e}(\boldsymbol{k})]_{NL} = -[\dot{e}(\boldsymbol{q})]_{NL}$ of (6) indicates that energy transfer is maximal within distant interactions when $\hat{\boldsymbol{u}}(\boldsymbol{k})$ and $\hat{\boldsymbol{u}}(\boldsymbol{q})$ are aligned.

Prediction. From these considerations, we predict that forcing will, over time, lead to an alignment of the real and imaginary vectorial components of $\hat{\boldsymbol{u}}(\boldsymbol{k})$ in those regions where distant interactions dominate the dynamics – that is, within the high-wavenumber modes near the k_x- and k_y-axes.

3.3. *Redistribution of small-scale component energy by forcing*

Consider the time rate of change in component kinetic energy within an arbitrary triadic interaction, given by

$$T_{\alpha\alpha}(\boldsymbol{k}) \equiv \frac{\mathrm{d}}{\mathrm{d}t}[\hat{u}_\alpha^*(\boldsymbol{k})\,\hat{u}_\alpha(\boldsymbol{k})]_{NL}, \quad [\dot{e}(\boldsymbol{k})]_{NL} = \sum_{\alpha=1}^{3} T_{\alpha\alpha}(\boldsymbol{k}), \tag{12}$$

where $$T_{\alpha\alpha}(\boldsymbol{k}) = 2\,\mathrm{Im}\{\hat{u}_\alpha^*(\boldsymbol{k})[\hat{\boldsymbol{u}}(\boldsymbol{q})_{\perp k}]_\alpha[\boldsymbol{k}\cdot\hat{\boldsymbol{u}}(\boldsymbol{p})] + \hat{u}_\alpha^*(\boldsymbol{k})[\hat{\boldsymbol{u}}(\boldsymbol{p})_{\perp k}]_\alpha[\boldsymbol{k}\cdot\hat{\boldsymbol{u}}(\boldsymbol{q})]\},$$

and $\boldsymbol{q} = \boldsymbol{k} - \boldsymbol{p}$. In the limit of infinite scale separation between a high-wavenumber mode $\boldsymbol{k}$ and a low-wavenumber mode $\boldsymbol{p}$, where $\delta \equiv p/k \sim p/q \ll 1$, equation (12) has the following form applicable to distant triadic interactions:

$$T_{\alpha\alpha}(\boldsymbol{k}) = 2\,\mathrm{Im}\{\hat{u}_\alpha^*(\boldsymbol{k})\,\hat{u}_\alpha(\boldsymbol{q})[\boldsymbol{k}\cdot\hat{\boldsymbol{u}}(\boldsymbol{p})]\} + O(\delta). \tag{13}$$

Note that the dot products in (12) indicate that, like $\dot{e}(\boldsymbol{k})$, $T_{\alpha\alpha}(\boldsymbol{k})$ is suppressed in the directions $\boldsymbol{p} = \pm \boldsymbol{k}_F^{(n)}$ at all $\boldsymbol{k}$, while (13) indicates that $T_{\alpha\alpha}(\boldsymbol{k})$ is suppressed also in the direction $\hat{\boldsymbol{e}}_z$ within distant interactions at high $\boldsymbol{k}$.

We ask now which components are most likely to receive energy within those dominant distant triadic interactions among the forced modes, $\pm \boldsymbol{k}_F^{(n)}$ and high-wavenumber modes near the k_x- and k_y-axes. Consider the distant interactions between $\boldsymbol{p} \equiv \pm \boldsymbol{k}_F^{(n)}$ and modes $\boldsymbol{k}$ and $\boldsymbol{q}$ near the k_x-axis. By continuity, $\hat{u}_\alpha^*(\boldsymbol{k})$ and $\hat{u}_\alpha(\boldsymbol{q})$ in (13) are non-zero only when $\alpha = 3$ or 2. Similarly distant triadic interactions between the forced modes and high-wavenumber modes lying near the k_y-axis can only move energy into the directions $\alpha = 3$ or 1.

Prediction. Because the distant interactions with the forced modes move energy into the z velocity component within high-wavenumber modes along both the k_x- and k_y-directions, we predict that component energy at the small scales will grow in the z-component relative to the x- and y-components.

3.4. *Timescales: relative effects of local-to-non-local and distant triadic interactions*

It was shown by Brasseur & Wei (1994) and Zhou (1993*a*, *b*) that the energy cascade from large to small scales is primarily within local and non-local triadic interactions with scale separation between roughly 1.5 and 10, with the most influential cascading interactions being those with scale separations up to roughly 5–7. Brasseur & Wei's analysis suggests that as energy moves from larger to successively smaller scales through local-to-non-local interactions, it becomes increasingly more uniformly distributed within spectral shells, thus leading to an increasingly isotropic distribution of energy with decreasing scale. The anisotropizing influence of the distant triadic group at the small scales, therefore, may be expected to be counteracted by the isotropizing influence of cascading 'local-to-non-local' triadic interactions. The timescale over which energy cascades to the small scales, however, is different from the small-scale response to distant triadic interactions with the energy-containing scales.

Consider the timescale $\tau(\boldsymbol{k})$ for energy transfer to or from mode $\boldsymbol{k}$ with energy $e(\boldsymbol{k})$:

$$\tau(\boldsymbol{k}) \sim e(\boldsymbol{k})/\dot{e}(\boldsymbol{k}), \tag{14}$$

where $e(\boldsymbol{k})$ and $\dot{e}(\boldsymbol{k})$ represent average values among modes within spectral shells centred on k. That is, we develop rough estimates for those timescales contributing to the rate of energy transfer within scales of motion $r \sim 1/k$ during interactions with other scales of motions. Consider, in particular, the timescale for energy transfer at the small scales due to a distant triadic intereaction, $\tau(\boldsymbol{k})_{distant}$, in comparison with the timescale associated with the cascade of energy from the large-scale forced mode $\boldsymbol{p} \equiv \boldsymbol{k}_F$, to small-scale modes $\boldsymbol{k}$, $\tau(\boldsymbol{k})_{cascade}$. Equation (5) implies $\dot{e}(\boldsymbol{k})_{distant} \sim k(e(\boldsymbol{p}))^{1/2} e(\boldsymbol{k})$, so that

$$\tau(\boldsymbol{k})_{distant} \sim (k[e(\boldsymbol{p})]^{1/2})^{-1}. \tag{15}$$

The timescale over which large-scale energy cascades to the small scales is governed by the number and timescales of multiple stages of non-local triadic interactions moving energy from larger to smaller scales. The timescale associated with single non-local interactions transferring energy to a higher-wavenumber mode $\boldsymbol{k}_L$ from a lower-wavenumber mode $\boldsymbol{k}_S$ is, from (9) and (14),

$$\tau(\boldsymbol{k}_L)_{non\text{-}local} \sim ([e(\boldsymbol{k}_S)\, e(\boldsymbol{k}_M)/e(\boldsymbol{k}_L)]^{1/2} k_L)^{-1}, \tag{16}$$

where $e(k)$ is the average mode energy in a shell of radius k, and $\boldsymbol{k}_S$, $\boldsymbol{k}_M$, $\boldsymbol{k}_L$ are the short-, medium- and long-wavenumber modes in a non-local energy-cascading interaction (i.e. subscripts S and L denote larger-scale and shorter-scale motions, respectively, in given triadic interactions). If the energy spectrum is given by $E(k) \sim k^{-m}$, then $e(k) \sim k^{-(m+2)}$ and

$$\tau(\boldsymbol{k}_L)_{non\text{-}local} \sim [\alpha\beta]^{-(m+2)/2} k_L^{m/2}, \tag{17}$$

where $k_L = \alpha k_S = \beta k_M$, $\alpha \geqslant \beta \geqslant 1$. For fixed α, a lower bound for $\tau(\boldsymbol{k})_{non\text{-}local}$ is given by maximum β. Since $\boldsymbol{k}_L$, $\boldsymbol{k}_M$ and $\boldsymbol{k}_S$ form a triangle, when $\alpha \geqslant 2$, $\beta_{max} = \alpha/(\alpha-1)$ and

$$\tau(\boldsymbol{k}_L)_{non\text{-}local} \sim \gamma k_L^{m/2}, \quad \text{where } \gamma = \left(\frac{\alpha^2}{\alpha-1}\right)^{-(m+2)/2} \quad (\alpha \geqslant 2); \tag{18}$$

γ decreases with increasing α (this is also true when $\alpha < 2$). As an example, if $m = \frac{5}{3}$ and $\alpha = 7$, $\tau(k_L)_{non\text{-}local} \sim 0.02 k_L^{5/6}$ (from the work of Brasseur & Wei 1994 and Zhou 1993*a*, *b*, $\alpha = 7$ is chosen as a maximal separation between dominant energy-cascading interactions).

It may be shown that the timescale for interscale energy transfer to the middle-wavenumber mode $\boldsymbol{k}_M$ is greater than $\tau(\boldsymbol{k}_L)_{non\text{-}local}$, so (18) is a lower bound for energy cascading triadic interactions. Because $\tau(\boldsymbol{k}_L)_{non\text{-}local}$ increases with increasing wavenumber, k_L, the minimum time required for energy to cascade from the large-scale forced modes at p to high-wavenumber modes at k is given by the final stage in the energy cascade, the non-local interactions which transport energy from $(1/\alpha)k$ to k ($k = k_L$ in equation (18)). Using (15) and (18), the minimum time for the energy cascade to high-wavenumber k may be compared with the timescale for energy exchange due to distant triadic interactions between low-wavenumber p and high-wavenumber k:

$$\frac{\tau(k)_{cascade}}{\tau(k)_{distant}} \sim \gamma (k/p)^{(m+2)/2} \quad \text{or greater}$$

$$\sim 0.02\,(k/p)^{11/6} \quad \text{for} \quad m = \tfrac{5}{3} \quad \text{and} \quad \alpha = 7. \tag{19}$$

In the current 128^3 simulations, $k/p \sim 10$–20 and $\tau(\boldsymbol{k})_{cascade}/\tau(\boldsymbol{k})_{distant} \sim 1.4$–$5$ or greater for $m = \frac{5}{3}$ and $\alpha = 7$. The ratio $\tau(\boldsymbol{k})_{cascade}/\tau(\boldsymbol{k})_{distant}$ increases rapidly with scale separation, k/p.

We conclude that the smallest scales respond to forcing within the distant triadic group before the energy cascade transports significant energy to the small scales, and that the difference in response time increases with scale separation. Furthermore, (15) indicates that, in general, the smaller the scale, the more rapid is the response from distant interactions to forcing. We have already argued (§3.1) that anisotropy induced at the small scales through the distant triadic group will be stronger at smaller scales. From the scaling arguments above, we now argue that within distant interactions the smallest scales respond to large-scale forcing first, followed by the next smallest scales, and so on.

Prediction. We predict, therefore, that small-scale *anisotropy* will appear *earlier* at *smaller scales*. We further predict that the level of anisotropy at the small scales will initially increase due to direct large–small scale interactions, then decrease at later time as large-scale energy from the forced modes reaches the small scales through local-to-non-local triadic interactions. Because the isotropizing influence of the energy cascade arrives from the large scales, the *reduction in anisotropy* will appear at the *larger scales first*, then proceed to successively smaller scales.

Because the ratio of timescales between the cascade of energy to the small scales and direct large–small scale interactions increases with scale separation, the effect of the distant group will be felt over longer time at larger Reynolds numbers since more time is required for energy to travel from large to small scales with greater scale separation.

It should be emphasized that the predictions in §3 follow from the asymptotic form of distant triadic interactions, applicable in the infinite Reynolds number limit. We

argue, therefore, that if the predicted response to forcing is demonstrated in the numerical experiments and if this response is shown to be a consequence of the most non-local and distant interactions, the effect is applicable also in the infinite Reynolds number limit.

4. Simulation details, analysis techniques, and the numerical experiment

4.1. *Simulation details and analysis techniques*

To simulate the response of isotropic turbulence to anisotropic forcing at the large scales, direct numerical simulations of the Navier–Stokes equations were carried out using Rogallo's (1981) pseudo-spectral algorithm for homogeneous turbulence. The particular version of code used in derived from that of Yeung & Pope (1988). The solution domain is a periodic cube of length $L = 2\pi$ with 128^3 equispaced grid points, so that the discrete wavevector components have integer values. Velocity fields in wavenumber space, from which velocity gradients can be readily calculated, are saved at selected time intervals for analysis.

Interscaling couplings arise from nonlinear terms in the Fourier-spectral Navier–Stokes equations. In Cartesian tensor notation, the continuous form of (2) may be written as

$$\left(\frac{\partial}{\partial t}+\nu k^2\right)\hat{u}_i(\boldsymbol{k},t) = -\frac{\mathrm{i}}{2}P_{ilm}(\boldsymbol{k})\int \hat{u}_l(\boldsymbol{p})\,\hat{u}_m(\boldsymbol{k}-\boldsymbol{p})\,\mathrm{d}\boldsymbol{p}, \tag{20}$$

where

$$P_{ilm}(\boldsymbol{k}) = k_m(\delta_{il}-k_i k_l/k^2)+k_l(\delta_{im}-k_i k_m/k^2). \tag{21}$$

Here δ_{ij} is the Kronecker delta tensor, and the usual summation convention applies. The energy and vorticity spectrum tensors are given by

$$E_{ij}(\boldsymbol{k}) \equiv \tfrac{1}{2}[\hat{u}_i(\boldsymbol{k})\,\hat{u}_j^*(\boldsymbol{k})+\hat{u}_i^*(\boldsymbol{k})\,\hat{u}_j(\boldsymbol{k})], \tag{22}$$

and

$$V_{ij}(\boldsymbol{k}) \equiv \tfrac{1}{2}[\hat{\omega}_i(\boldsymbol{k})\,\hat{\omega}_j^*(\boldsymbol{k})+\hat{\omega}_i^*(\boldsymbol{k})\,\hat{\omega}_j(\boldsymbol{k})], \tag{23}$$

where $\hat{\boldsymbol{\omega}}(\boldsymbol{k})$, the Fourier transform of the vorticity field $\boldsymbol{\omega}(\boldsymbol{x})$, is given by $-\mathrm{i}\boldsymbol{k}\times\hat{\boldsymbol{u}}(\boldsymbol{k})$. (Note that $\hat{\boldsymbol{u}}^*(\boldsymbol{k}) = \hat{\boldsymbol{u}}(-\boldsymbol{k})$ and $E_{ii}(\boldsymbol{k})$ is the same as $e(\boldsymbol{k})$ in equation (3).) The energy spectrum tensor evolves according to

$$\frac{\partial E_{ij}(\boldsymbol{k})}{\partial t} = T_{ij}(\boldsymbol{k})-2\nu k^2 E_{ij}(\boldsymbol{k}), \tag{24}$$

where intercomponent and interscale energy transfer is represented by the transfer spectrum tensor,

$$T_{ij}(\boldsymbol{k}) = \tfrac{1}{2}\,\mathrm{Im}\left([P_{ilm}(\boldsymbol{k})\,\hat{u}_j^*(\boldsymbol{k})+P_{jlm}(\boldsymbol{k})\,\hat{u}_i^*(\boldsymbol{k})]\int \hat{u}_l(p)\,\hat{u}_m(\boldsymbol{k}-\boldsymbol{p})\,\mathrm{d}\boldsymbol{p}\right). \tag{25}$$

While (20) and (25) contain convolution integrals which can be evaluated efficiently by a pseudo-spectral method with number of operations scaling as $N^3 \ln N$, where N is the number of grid points in each coordinate direction, the pseudo-spectral approach does not provide direct information on individual triadic interactions. On the other hand, whereas the triad-geometrical formulation of (2) and (3) as a discrete sum over triadic interactions is computationally expensive with the number of operations $\sim N^6$, it is feasible if a small dynamically significant subset of triadic interactions is computed (Brasseur & Wei 1994), and will be used to advantage in §7 to study the effects of geometrical properties of the triads on energy transfer.

The spectra $E_{ij}(\boldsymbol{k})$, $T_{ij}(\boldsymbol{k})$ and $V_{ij}(\boldsymbol{k})$ integrated over spectral shells of radius k and unit thickness to give the radial spectrum tensors $E_{ij}(k)$, $T_{ij}(k)$ and $V_{ij}(k)$. Half the traces of $E_{ij}(k)$ and $T_{ij}(k)$ give the radial energy and transfer spectrum functions $E(k)$ and $T(k)$, respectively.

Contributions to the energy transfer within a spectral shell from different spectral shells in wavenumber space are conveniently represented using the formalism introduced by Domaradzki & Rogallo (1990), where $T(k\,|\,p)$ is defined as the transfer of energy to wavenumbers k due to triads with at least one leg in a spherical shell centred on p. Similarly, $T(k\,|\,p,q)$ is defined as energy transfer to k due to triads with one leg in a shell centred on p and the other leg in a shell centred on q. These definitions imply the relationships

$$T(k) = \sum_p T(k\,|\,p) = \sum_p \left[\sum_q T(k\,|\,p,q) \right]. \tag{26}$$

Similar relations hold for the component transfer spectra $T_{\alpha\alpha}(\boldsymbol{k})$ (see YB).

To quantify scale-dependent features of turbulence statistics in physical space, various correlations between band-pass-filtered variables are carried out in §9 (e.g. She, Jackson & Orszag 1988). For chosen sets of Fourier modes $\mathscr{L}$ and $\mathscr{H}$ specifically, the filtered velocity and vorticity fields are defined by $\boldsymbol{u}(\boldsymbol{x}\,|\,\mathscr{L})$ and $\boldsymbol{\omega}(\boldsymbol{x}\,|\,\mathscr{H})$ which have Fourier transforms

$$\hat{\boldsymbol{u}}(\boldsymbol{k}\,|\,\mathscr{L}) = \begin{cases} \hat{\boldsymbol{u}}(\boldsymbol{k}) & \boldsymbol{k} \in \mathscr{L} \\ 0\,, & \text{otherwise}\,, \end{cases} \tag{27}$$

and

$$\hat{\boldsymbol{\omega}}(\boldsymbol{k}\,|\,\mathscr{H}) = \begin{cases} \hat{\boldsymbol{\omega}}(\boldsymbol{k}) & \boldsymbol{k} \in \mathscr{H} \\ 0\,, & \text{otherwise}\,, \end{cases} \tag{28}$$

where $\mathscr{L}$ and $\mathscr{H}$ are specified spectral shells.

Whereas to quantity scale-dependent effects unambiguously in physical space band-pass filtering is useful, to visualize scale-dependent physical-space structure, the wavelet transform provides a more useful filtering technique (see Brasseur & Wang 1992; Wang & Brasseur 1993; Wang *et al.* 1994). One advantage of the wavelet filter is that the resulting transform has a clear interpretation also in physical space as the convolution of a stretched 'wavelet' $g(\boldsymbol{x})$ with a signal $\phi(\boldsymbol{x})$:

$$\Phi(\boldsymbol{\xi}, a) = w(a) \int_{-\infty}^{\infty} g^*\left(\frac{\boldsymbol{x}-\boldsymbol{\xi}}{a}\right) \phi(\boldsymbol{x})\, \mathrm{d}\boldsymbol{x}, \tag{29}$$

where a is the wavelet scale and $w(a)$ is an arbitrary weighting function used to accentuate different scales (see Combes, Grossman & Tchamitchian 1989; Brasseur & Wang 1992; Wang *et al.* 1994). The function $g(\boldsymbol{x})$ must be square integrable and therefore of finite support. Consequently $\Phi(\boldsymbol{\xi}, a)$ contains information from a localized region of scale a surrounding $\boldsymbol{\xi}$, the details of which depend on the form of the wavelet $g(\boldsymbol{x})$. In this sense the wavelet transform is quasi-local in physical space.

The Fourier transform of (29) is (Wang *et al.* 1994)

$$\hat{\Phi}(\boldsymbol{k}, a) = w(a)\, a^3 \hat{g}^*(a\boldsymbol{k})\, \hat{\phi}(\boldsymbol{k}), \tag{30}$$

where $\phi(\boldsymbol{k})$ and $\hat{g}(\boldsymbol{k})$ are the Fourier transforms of $\phi(\boldsymbol{x})$ and $g(\boldsymbol{x})$, respectively, showing that the wavelet transform is a scale-dependent spectral filter given by $\hat{g}(a\boldsymbol{k})$. Because $g(\boldsymbol{x})$ has zero mean, $\hat{\Phi}(\boldsymbol{k}, a)$ contains information from a localized region in Fourier space surrounding the peak in $\hat{g}(a\boldsymbol{k}), \boldsymbol{k}_a$; both $|\boldsymbol{k}_a|$ and the support of $\hat{g}(a\boldsymbol{k})$ surrounding $\boldsymbol{k}_a$ scale with $1/a$. Consequently, the quasi-locality of $\Phi(\boldsymbol{\xi}, a)$ in physical

space translates directly to a quasi-locality of $\hat{\Phi}(\boldsymbol{k}, a)$ in Fourier space such that the more extended the wavelet is surrounding $\boldsymbol{\xi}$ in physical space, the more local is the wavelet filter surrounding $\boldsymbol{k}_a$ in Fourier space, and vice versa.

In this study the 'Mexican-hat' wavelet transform is applied to the vorticity vector field, $\phi(\boldsymbol{x}) \equiv \omega_i(\boldsymbol{x})$, where

$$g(\boldsymbol{x}) = -\nabla^2 \mathrm{e}^{-x^2} = (3 - x^2)\mathrm{e}^{-x^2}, \tag{31}$$

and $x^2 \equiv \boldsymbol{x} \cdot \boldsymbol{x}$. The Mexican hat wavelet is spherically symmetric in both physical space (equation (31)) and Fourier space:

$$\hat{g}(\boldsymbol{k}) = (2\pi)^{3/2} k^2 \mathrm{e}^{-k^2/2} = \hat{g}(k). \tag{32}$$

The wavelet filter $\hat{g}(ak)$ selects Fourier modes dominantly near the peak in $\hat{g}(ak)$ which, for the Mexican-hat wavelet is at $k_a = \sqrt{2}/a$. Decreasing the wavelet scale is equivalent to shifting the peak of the wavelet filter to select from higher-wavenumber spectral shells, and increasing the range of Fourier modes filtered. Further details of the wavelet transform and its application as a spectral filter are given in Brasseur & Wang (1992) and Wang *et al.* (1994).

4.2. *The numerical experiment*

In our numerical experiment, initially isotropic turbulence is forced coherently within a 4×4 array of counter-rotating vortex tubes aligned with the z-axis which is highly localized at the large scales. The method of forcing is the same as in our earlier work (YB) and is described there in detail. A steady extra forcing term is added to the Fourier-space Navier–Stokes equation (20) through which energy and vorticity are added at a constant rate to the two-component velocity field and one-component vorticity shown in figure 3. Stagnation points are formed in the forcing velocity field at locations equidistant from sets of four adjacent spanwise vortex cores. Although the forcing term is held fixed in time, the rates of increase of energy and enstrophy due to forcing change with time as shown in YB.

The distribution of vorticity within the forcing vortices is based on an expression devised by Melander, McWilliams & Zabusky (1987). The size and geometrical arrangement of the 16 vortices, as shown in figure 3, are such that 99.4% of the energy of the vortical forcing field is shared equally by the two pairs of Fourier modes of equal magnitude in figure 2 with wavevector components $(\pm 2, \pm 2, 0)$. Forced energy enters the Fourier coefficients $\hat{\boldsymbol{u}}(\boldsymbol{k}_F) = \mathrm{i}\boldsymbol{b}(\boldsymbol{k}_F)$ only through their imaginary parts, $\boldsymbol{b}(\boldsymbol{k}_F)$, where $\boldsymbol{b}(\boldsymbol{k}_F)$ are confined to the (k_x, k_y)-plane as shown in figure 2. The lengths of these vectors increase rapidly with time upon initiation of forcing.

In the following sections, we present and discuss the effects of continuous large-scale vortical forcing on initially fully developed isotropic turbulence over a period of about 6 initial eddy-turnover times (defined using the initial integral lengthscale and r.m.s. velocity component).

5. Transition from decaying isotropic turbulence to a state of non-equilibrium

Here we examine the evolution of global statistics and anisotropy of initially isotropic turbulence at various scales in response to coherent non-isotropic forcing in a narrow shell $k_F = 2\sqrt{2} = 2.83$, as described in the previous section. The initial state of fully developed isotropic turbulence is obtained by simulating natural isotropic decaying turbulence from a Gaussian velocity field using 128^3 computational nodes. The initial isotropic state, the same as in YB, has a Taylor-scale Reynolds number of

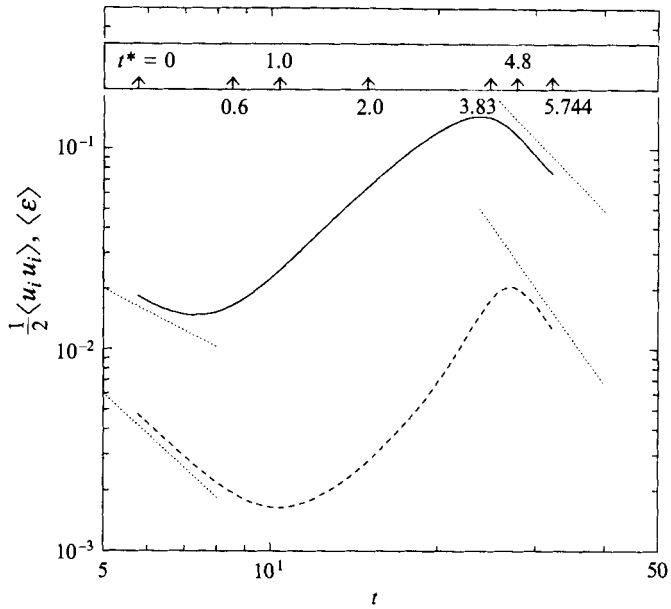

FIGURE 4. Temporal evolution of global mean kinetic energy (solid line) and dissipation rate (dashed line) during continuous forcing. A period of non-equilibrium restructuring takes place between two periods of decay. Initial and final slopes representing power laws are -1.42 and -2.91 respectively for energy, and -2.51 and -3.89 for dissipation rate. Selected values of non-dimensional time $t^* = (t-5.7645)/T_E$ are also indicated, where $t^* = 0$ is the initiation of forcing and T_E is the large-eddy timescale in the initial isotropic state.

20 and an eddy-turnover time $T_E = 4.60$ with kinematic viscosity $\nu = 0.001\,377$ (units must be consistent, but may be chosen arbitrarily). The peaks in the energy and dissipation rates at forcing are near $k_E \approx 3$ and $k_D \approx 12$, respectively, with the highest resolved wavenumber k_{max} being 60 for a 128^3 grid. Both the largest and smallest scales are well resolved. When large-scale forcing is initiated, $L/l = 11.5$, where L is a box dimension and l is the integral scale; and $k_{max}\eta = 1.63$, corresponding to $\eta/\Delta = 0.55$, where η is the Kolmogorov scale and Δ the grid spacing. During the course of simulation $k_{max}\eta$ varies between 1.1 and 2.1, meeting the generally accepted criterion $k_{max}\eta > 1$ for adequate resolution of the small scales (Yeung & Pope 1989).

Continuous forcing causes the energy and dissipation rate to deviate from an equilibrium isotropic state of power-law viscous decay. Figure 4 shows the evolution of mean kinetic energy, $\frac{1}{2}\langle u_i u_i \rangle$, and dissipation rate, $\langle \epsilon \rangle$, over a period of 5.744 initial eddy-turnover times beyond the initiation of forcing (three times longer than the previous simulations in YB). The ensemble averages (in angle brackets) here are space averages over the box. Both quantities deviate only slightly from power laws in the early stages of forcing, but subsequently increase with time as the turbulence enters a non-equilibrium period of rapid change. Because the forcing modes are at low wavenumbers which contribute more to energy than to dissipation rate, energy response earlier to forcing and begins to increase about $0.6T_E$ earlier than the dissipation rate. As a large spike in energy develops at low wavenumbers due to forcing, these same low-wavenumber modes gradually become major contributors to the dissipation rate also. In fact, the spectral shell $2.5 \leqslant k < 3.5$, which contains the forced modes, contributes 82% to the energy and 43% to the dissipation rate at about $2T_E$ after initiation of forcing, far higher than the 9% and 1%, respectively, at the

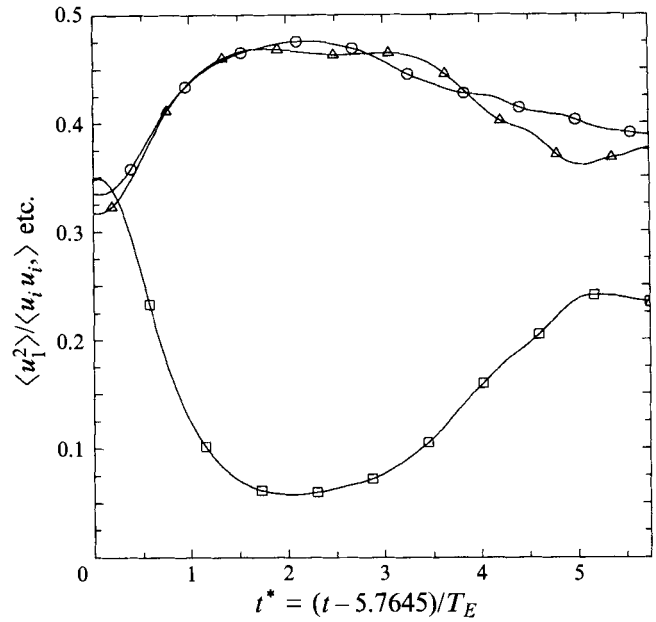

FIGURE 5. Component energies during forcing normalized by twice total energy, shown against non-dimensional time after initiation of forcing (t^* in figure 4). △, ○, □ show the x-, y-, z-components respectively.

initial isotropic state. Consequently, at intermediate times energy and dissipation rate evolve in a similar manner.

Near the end of the simulation, the data show the tendency for a second power-law regime with rapid decay after the greatly increased total kinetic energy has become overwhelmed by greatly increased dissipation of kinetic energy at the small scales (e.g. compare component spectra in figure 8*d* and figure 8*a*). These global measures suggest the existence of three global periods of turbulence evolution which are relevant to this study: (i) the initial isotropic state of equilibrium decay is disturbed by continuous forcing at the large scales; (ii) the turbulence then evolves through a non-equilibrium period of transient change before (iii) reaching what appears to be a new quasi-equilibrium state of decay at higher energy level.

Prolonged continuous forcing leads eventually to oscillations in kinetic energy and dissipation rate. We do not analyse the flow beyond the second quasi-equilibrium period. Because this second equilibrium state results from continuous anisotropic forcing at the larger scales, the small-scale turbulence structure is found to be different from the initial period of isotropic decay.

In figure 4 we use the same arbitrary time t as in YB, with Gaussian initial conditions specified at $t = 0$. In addition, we have indicated some events in non-dimensional time t^* with the origin shifted to the initiation of forcing ($t = 5.7645$) and time normalized by the initial eddy-turnover time T_E. With the exception of figure 4, all results will be given in non-dimensional time ($0 \leqslant t^* \leqslant 5.744$). Note that the non-equilibrium period of adjustment to forcing ends near $t^* \approx 4.8$.

The u_1 and u_2 velocity components gain energy directly from forcing, while u_3 is affected only through nonlinear interactions. Component energy ratios are plotted against time in figure 5, indicating that the forced turbulence is in an overall axisymmetric state in which $\langle u_1^2\rangle \approx \langle u_2^2\rangle > \langle u_3^2\rangle$. Global anisotropy reaches a

maximum near $t^* \approx 2$, but then decreases, even while forcing continues. Anisotropy due to the forcing is seen to be transient, although the return to isotropy is slower than if forcing were terminated as in YB. Note that the minimum large-scale anisotropy level is reached at the apparent end of the transient periods of non-equilibrium adjustment displayed in figure 4 ($t^* \sim 4.8$–5.0).

6. Temporal development of anisotropy at different scales in the spectral view

The anisotropy of the turbulent fluctuations has a strong scale dependence which can be quantified by the anisotropy of the radial energy spectrum tensor:

$$A_{ij}(k) = \frac{E_{ij}(k)}{E_{nn}(k)} - \tfrac{1}{3}\delta_{ij}, \tag{33}$$

where $E_{ij}(k)$ is given by integrating $E_{ij}(\boldsymbol{k})$ over a sphere of radius k. The extent to which the velocity fluctuations are anisotropic at scale $r \sim 1/k$, is quantified by the deviation of $A_{ij}(k)$ from zero, which itself is given by its three principal invariants $\mathrm{I}_A(k) = A_{ii}(k) \equiv 0$, $\mathrm{II}_A(k) = \frac{1}{2}A_{ij}(k)\,A_{ji}(k)$ and $\mathrm{III}_A(k) = \frac{1}{3}A_{ij}(k)\,A_{jn}(k)\,A_{ni}(k)$ (Lumley & Newman 1977; the latter two expressions require $\mathrm{I}_A = 0$). Whereas $\mathrm{III}_A(k) \neq 0$ necessarily implies $\mathrm{II}_A(k) \neq 0$ but not vice versa, we have found $\mathrm{II}_A(k)$ and $\mathrm{III}_A(k)$ to be equally good measures of anisotropy in $E_{ij}(k)$. However, whereas $\mathrm{II}_A(k) \geqslant 0$ measures the magnitude of $A_{ij}(k)$, $\mathrm{III}_A(k)$ may be positive or negative and, as such, includes some information on structure at scale k.

It is important to recognize that whereas non-zero $A_{ij}(k)$ necessarily implies some level of anisotropy in scales surrounding k, the converse is not true in general. As we shall show in §10, the return of $E_{ij}(k)$ to isotropy does not necessarily imply an isotropic structure in the turbulence. In principle, all order moments must be isotropic (Kolmogorov 1941).

$\mathrm{III}_A(k)$ is plotted for different times during forcing from $t^* = 0$ to 3.830 in figure 6. Immediately after forcing, the forced large scales develop negative $\mathrm{III}_A(k)$ which follows from the two-component nature of forcing. Small-scale anisotropy develops rapidly between curves D and F ($t^* \sim 1.6$–1.9), in response to the large-scale forcing, before decreasing at later times. It was shown in YB that this development of anisotropy at the small scales is a direct consequence of the highly non-local and distant triadic interactions among small-scale modes and the forced modes $\pm \boldsymbol{k}_F^{(n)}$. An important observation from figure 6 is that small-scale anisotropy develops with the sign of $\mathrm{III}_A(k)$ opposite to large-scale forced aisotropy, indicating an induced anisotropic small-scale structure which is different from the forced structure at the large scales. Especially important is the observation that the induced small-scale anisotropy is progressively greater at smaller scales, consistent with asymptotic arguments in §3.1. Small-scale anisotropy, however, changes more rapidly with time than large-scale anisotropy.

This last point is made evident by plotting $\mathrm{III}_A(k)$ against time within different spectral shells, figure 7. The numerical oscillations in figure 6, a result of the limited numbers of very low-wavenumber samples in shells of unit thickness, and low energy at very high wavenumbers, are smoothed in figure 7 by using wider wavenumber shells. Note that anisotropy in the forced scales (curve A) develops within one initial eddy turnover time (T_E) while the small scales (curves C–K) require about one T_E to respond to large-scale forcing. For fixed time, anisotropy increases monotonically with wavenumber (shells C, D, E,...) in shells $k > 10$, again consistent with discussions in

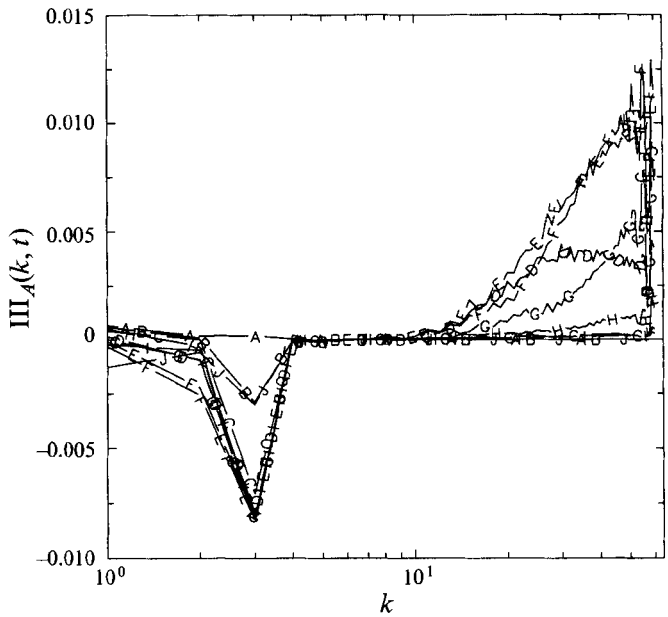

FIGURE 6. Third anisotropy invariant of the energy spectrum tensor versus wavenumber, at different times during forcing. Non-dimensional times $t^* = 0$ (A), 0.479 (B), 0.957 (C), 1.436 (D), 1.676 (E), 1.915 (F), 2.393 (G), 2.872 (H), 3.351 (I) and 3.830 (J). Whereas the anisotropy of $E_{ij}(k)$ at the small scales is near zero for t^* later than 3.5, the small scales are not isotropic (discussed in §10).

§3.1. As importantly, note from the expanded view in figure 7(*b*) that the highest-wavenumber shells (H–K) respond first to forcing, followed by successively lower-wavenumber shells. This result is consistent with the prediction in §3.4 where it was argued based on the asymptotic form of the triadic equations that small-scale anisotropy should appear earlier at smaller scales.

It was also argued in §3.4 that a reduction in small-scale anisotropy can be expected at later times in response to the cascade of energy from the large-scale forced modes, and that the reductions in $\mathrm{III}_A(k)$ should begin at larger scales and proceed to small scales. This is precisely the behaviour observed in figure 7(*a–c*). Note that in each shell anisotropy increases then decreases with time. Peak anisotropy (figure 7*a*) and subsequent reduction in anisotropy (figure 7*c*) shifted to later time at smaller scales. From the timescale arguments in §3.4, this shift to later time is a reflection of the isotropizing influence of energy-cascading local-to-non-local triadic interactions which moves from large to small scales, counteracting the anisotropizing influence of distant-to-highly-non-local triadic interaction which moves from the smallest scales to larger scales.

Note the monotonic increase in the peak value of $\mathrm{III}_A(k)$ with k. This, we argue, is a consequence both of the greater influence of the forced modes on smaller scales through distant triadic interactions (§3.1), and the greater time required for the isotropizing influence of energy-cascading interactions to arrive at smaller scales (§3.4). The return to nearly total isotropy in $E_{ij}(k)$ in all high-wavenumber shells C–K while significant anisotropy remains in low-wavenumber shell A was initially unexpected. It turns out, however, that the return to isotropy at $t^* \approx 3.5$ in figure 7 is only illusory. As we shall see in §10, a reduced level of anisotropy exists at the small scales at for $t^* > 3.5$ which is not detected in $E_{ij}(k)$ but is apparent from visualizations of enstrophy or energy isosurfaces in Fourier space and the physical space. The anisotropy is such

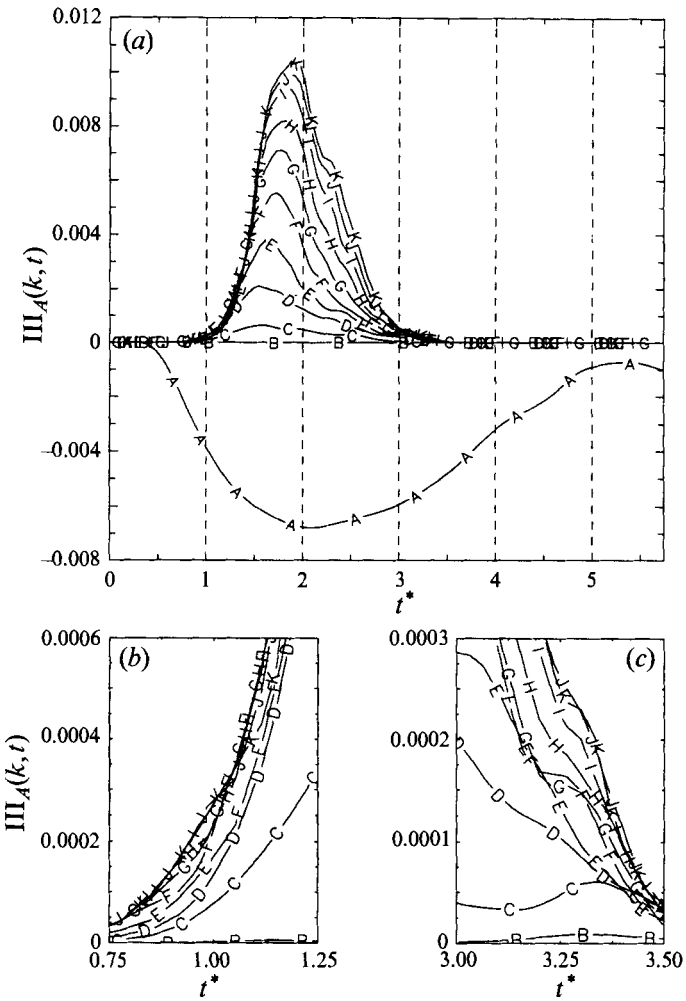

FIGURE 7. Third anisotropy invariant of the band-pass energy spectrum tensor versus non-dimensional time from $t^* = 0$ to 5.744, for different wavenumber bands of thickness 5 units centred in the following wavenumbers: 3 (A), 8 (B), 13 (C), 18 (D), 23 (E), 28 (F), 33 (G), 48 (H), 43 (I), 38 (J), 53 (K). (*b*) and (*c*) are expanded views showing the periods in which small-scale anisotropy in $E_{ij}(k)$ begins to develop and disappear, respectively. However, whereas the anisotropy of $E_{ij}(k)$ at the small scales is near zero for $t^* \gtrsim 3.5$, we show in §10 that the small scales are not isotropic.

that $E_{ij}(k)$ is unresponsive to the turbulence structure, and to quantify small-scale anisotropy statistically, high-order moments are necessary.

Figure 8 shows the evolution of the energy and vorticity spectra at intervals of approximately 2 initial eddy-turnover times. Note that at $t^* \approx 2$ the flow is dominantly two-component in velocity and one-component in vorticity at the large scales $(u_x, u_y; \omega_z)$, but one-component in velocity and two-component in vorticity at the small scales $(u_z; \omega_x, \omega_y)$. We shall show in §§7 and 8 that the small-scale vorticity field is dominated by vortices aligned in the x- and y-directions which are associated with the dominantly spanwise velocity field.

Anisotropy-invariant maps (not shown) have been obtained for the Reynolds-stress, vorticity-correlation and dissipation-rate tensors representing velocity and vorticity fields filtered in wavenumber space. Consistent with figure 8, the invariant paths of

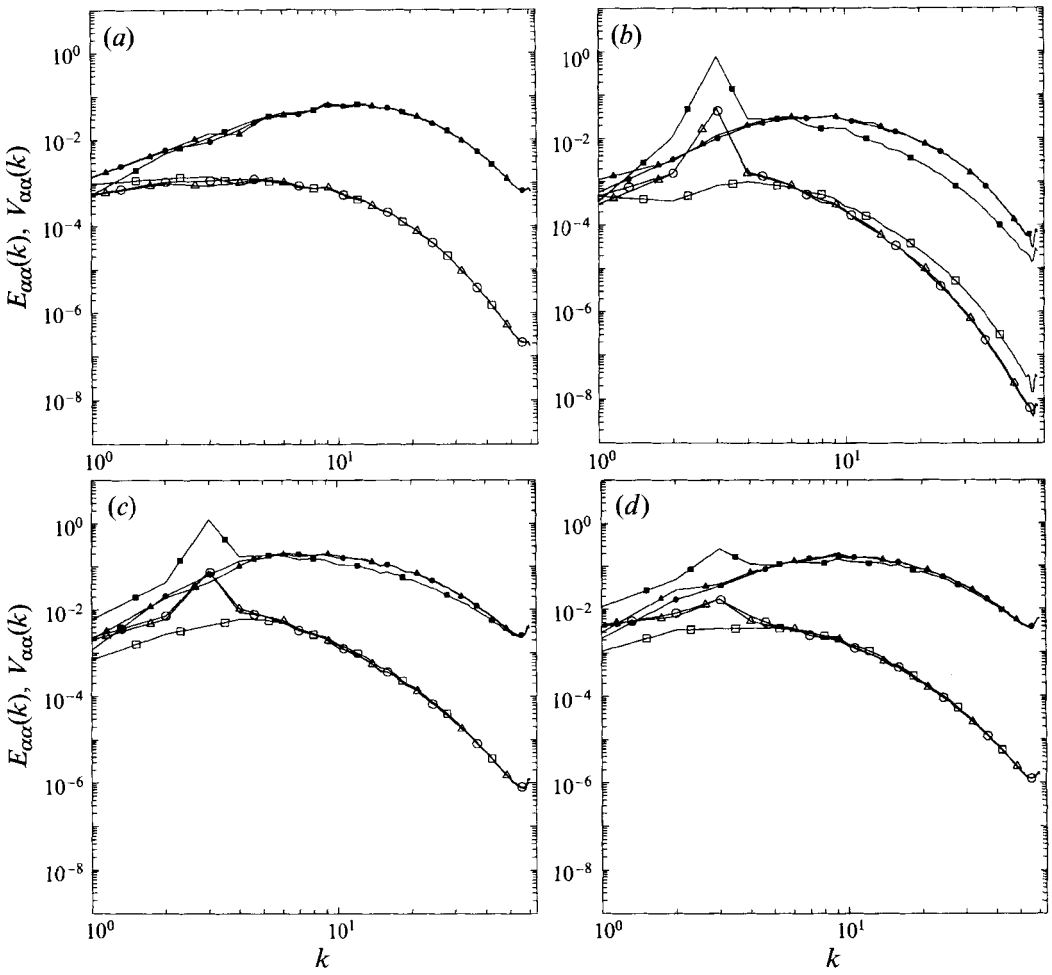

FIGURE 8. Radial component spectra of energy and enstrophy components ($E_{\alpha\alpha}(k)$ and $V_{\alpha\alpha}(k)$, no sum on α) versus wavenumber roughly every 2 eddy-turnover times: (*a*) $t^* = 0$; (*b*) 1.915; (*c*) 3.830; and (*d*) 5.744. Open symbols are △, $E_{11}(k)$; ○, $E_{22}(k)$; □, $E_{33}(k)$. Corresponding closed symbols for enstrophy component spectra.

filtered $A_{ij}(k)$ indicate that the forced turbulence remains axisymmetric at all scales throughout the simulation.

7. Three-dimensional restructuring of Fourier space by large–small scale non-cascading interactions: comparisons with the asymptotic limit

A number of predictions were made in §§3.1–3.3 concerning the redistribution of energy, component energy and phase at the small scales as a direct consequence of large–small scale interactions during coherent forcing at the large scales. We discuss the details of this high-wavenumber restructuring and compare it with these predictions in this section. We find that large–small scale interactions lead to well-defined regions in wavenumber space where spectral energy and vorticity are concentrated and in which a high degree of phase coupling exists among the Fourier modes. We show in §8 that a direct correspondence exists between these regions of concentrated activity in Fourier space and the structure of the vorticity field in physical space.

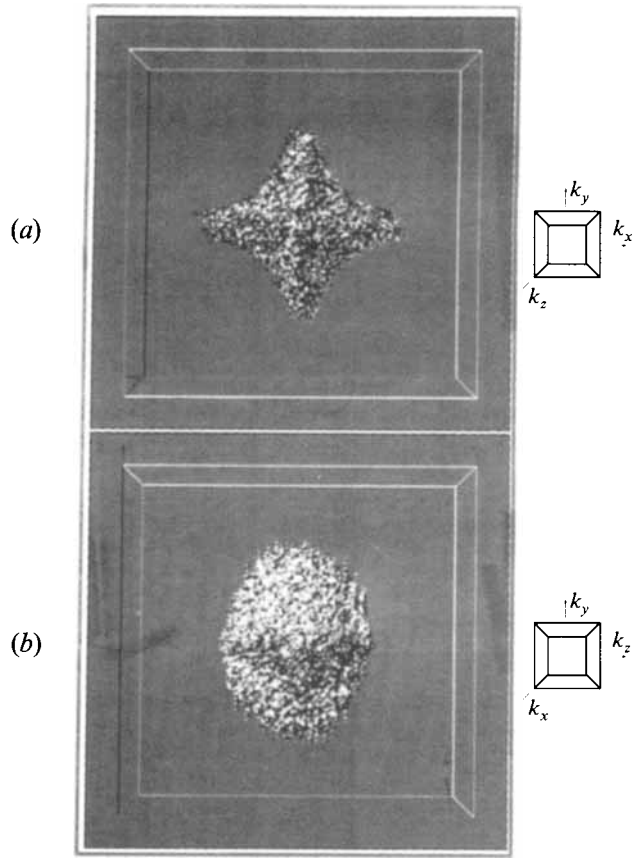

FIGURE 9. Three-dimensional isosurfaces of enstrophy in Fourier space, $\hat{\omega}_i(\boldsymbol{k})\,\hat{\omega}_i^*(\boldsymbol{k})$, for the forced turbulence at peak small-scale anisotropy in figure 7, $t^* = 1.915$. The isosurface level is 0.001 r.m.s. above the mean value of the total enstrophy field. (*a*) Front view, looking down the k_z-axis; (*b*) side view, looking along the k_x-axis. Note the anisotropic distribution of enstrophy (and energy) in both views.

7.1. *Redistribution of small-scale spectral energy*

It was argued in §3.1 that, based on the asymptotic form of the triadic equations at large scale separation, distant triadic interactions among the forced modes and smallest scales will lead to a redistribution of mode energy $E_{ii}(\boldsymbol{k}) \equiv e(\boldsymbol{k})$ at the small scales whereby $E_{ii}(\boldsymbol{k})$ will concentrate around the k_x- and k_y-axes and be depleted in the directions of the forced modes $\pm\boldsymbol{k}_F^{(n)}$ and k_z (see figure 2). We further argued that the distant triadic response would be stronger and the predicted restructuring of $E_{ii}(\boldsymbol{k})$ would be more apparent at smaller scales.

To see that the restructuring predicted from the triadic group does take place in the simulation, compare figure 1 with figure 9. Figure 1(*b*) shows a single isosurface of $E_{ii}(\boldsymbol{k})$ at high wavenumbers ($k \sim 40$) in the isotropic state, just before forcing. Figure 9 shows the distortion in the high-wavenumber isosurface at $t^* = 1.915$, when small-scale anisotropy is maximum (figure 7). In the isotropic state, the isosurface is spherical. Large-scale forcing through $\pm\boldsymbol{k}_F^{(n)}$ has distorted the isosurface such that high-wavenumber spectral energy concentrates near the k_x- and k_y-axes. The depletion of energy in the $\pm\boldsymbol{k}_F^{(n)}$ directions are apparent in figure 9(*a*) as depressions in the isosurface at 45° to k_x,- k_y- and k_z-axes. The depletion of energy in the k_z-direction is

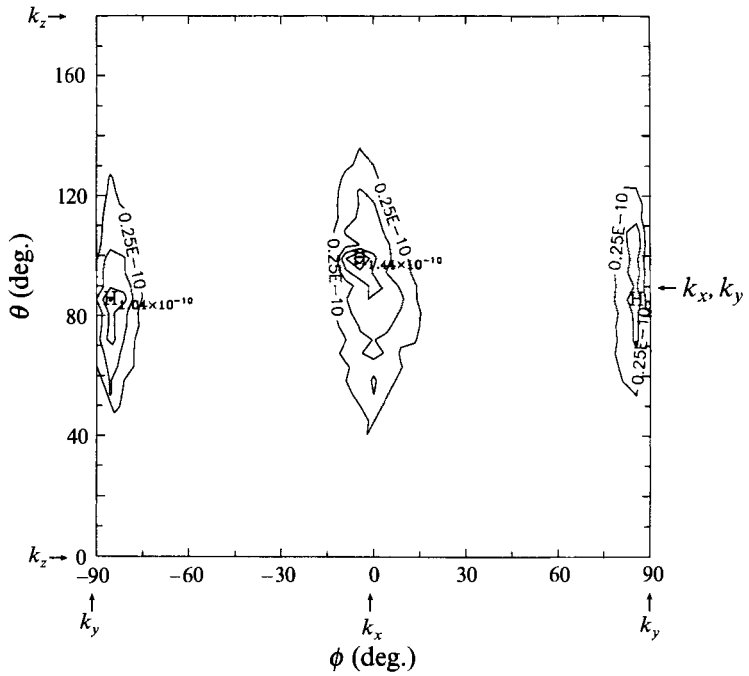

FIGURE 10. Isocontours of the spectral distributions of turbulent kinetic energy $E_{ii}(\boldsymbol{k})$ within the high-wavenumber shell $40 \leqslant k < 50$ at peak anisotropy, $t^* = 1.915$. The spherical coordinates are defined in figure 11.

shown in figure 9(*b*) as a distortion of the isosurface in the (k_y, k_z)-plane from circular to ellipsoidal. Finally, these figures show that the response predicted by the distant group in equation (10) is stronger at smaller scales in that the concentration of $E_{ii}(\boldsymbol{k})$ around k_x and k_y is more apparent at higher wavenumbers.

Details of the non-isotropic structure of mode energy at high wavenumbers is shown in spherical coordinates in figure 10, where the spherical coordinates are defined as figure 11. In figure 10 the annular region $40 \leqslant k \leqslant 50$ is divided into 40×40 uniform sampling bins in ϕ and θ and local energy computed in each bin. Modes in this bin form marginally distant triads with forced modes with scale ratio between 14.1 and 18.7. Because the Fourier mode energy is symmetric about the origin, only the $k_x > 0$ modes $(-\pi/2 \leqslant \phi < \pi/2)$ are shown. Note the highly non-uniform energy distribution in figure 10. Very low energy exists within 40° to the k_z-axis ($\theta = 0°, 180°$) or in the directions of the forced low-wavenumber modes ($\theta = 90°, \phi = \pm 45°$). Energy is highly concentrated in ellipsoidal regions surrounding the k_x- and k_y-axes, where the ellipsoid is roughly three times longer in the k_z direction than in the (k_x, k_y)-plane.

The redistribution of energy at high wavenumbers from large-scale forcing is a direct consequence of the marginally distant triadic interactions in the simulation and follows the prediction in §3.1 from consideration of the distant triadic equations. We show now that the distant interactions also lead to phase couplings among the high-wavenumber Fourier modes.

7.2. *Redistribution of small-scale phase*

The small-scale evolution of the velocity, vorticity, strain rate, etc. in physical space, as described by equation (4), involves both the redistribution of energy and phase among those Fourier modes which characterize the small scales, where 'phase' is related to the orientations and relative magnitudes of the real and imaginary parts of

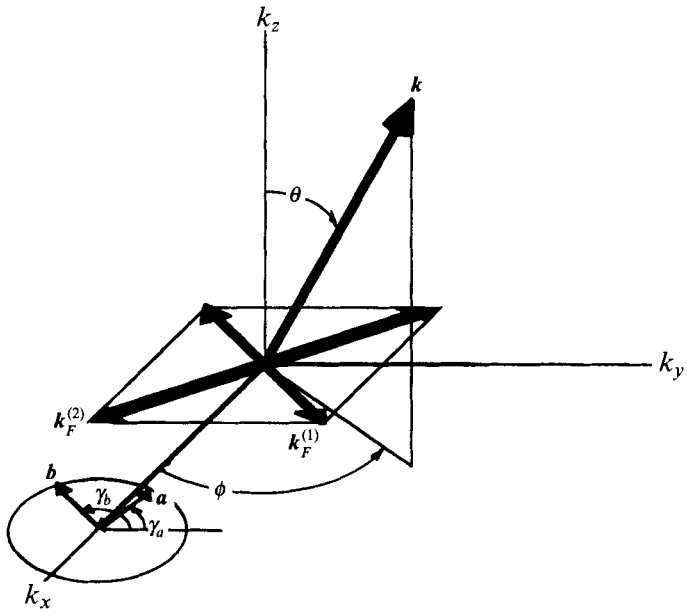

FIGURE 11. Schematic illustration of the spherical coordinate system $\boldsymbol{k} = (k, \theta, \phi)$ used in discussions of the energy and vorticity distribution within spectral shells. The directly forced modes are $\pm\boldsymbol{k}_F^{(1)}$ and $\pm\boldsymbol{k}_F^{(2)}$ shown with their lengths exaggerated. Also shown are the definitions of the azimuthal angles γ_a and γ_b in the (k_x, k_z)-plane of the real and imaginary parts $(\boldsymbol{a}, \boldsymbol{b})$ of the complex Fourier coefficients, discussed in §7.2 (figure 12).

the Fourier coefficients. Here we show that, in response to coherent large-scale forcing, direct interactions with the large scales through the distant triadic group cause a realignment in the orientation of the Fourier coefficients consistent with the prediction in §3.2 – namely, that $\boldsymbol{a}(\boldsymbol{k})$ and $\boldsymbol{b}(\boldsymbol{k})$ in the more energetic high-wavenumber regions are forced to align by distant interactions with the large-scale forced modes, where $\hat{\boldsymbol{u}}(\boldsymbol{k}) = \boldsymbol{a}(\boldsymbol{k}) + \mathrm{i}\boldsymbol{b}(\boldsymbol{k})$. In addition, we find that the alignment is in a particular direction which is directly associated with structure of the vorticity field in physical space (§8).

Consider, for example, the Fourier modes within the most energetic region surrounding the k_x-axis in the high-wavenumber shell $40 \leqslant k < 50$. With reference to figure 10, we choose the modes within $50° \leqslant \theta < 130°$ and $0° \leqslant |\phi| < 20°$, a conical region surrounding the k_x-axis. Let γ_a and γ_b be the azimuthal angles of $\boldsymbol{a}$ and $\boldsymbol{b}$ measured from the k_x-axis in the (k_x, k_z)-plane as shown in figure 11 ($\gamma_a = \arctan(a_3/a_2)$ and $\gamma_b = \arctan(b_3/b_2)$; note that $\boldsymbol{a}(\boldsymbol{k})$ and $\boldsymbol{b}(\boldsymbol{k})$ are perpendicular to $\boldsymbol{k}$). A correlation in phase among the Fourier modes implies a correlation in γ_a and γ_b among the Fourier modes within the energetic spectral regions.

In figure 12, the p.d.f.s of γ_a and γ_b are plotted for those modes in the energetic high-wavenumber region around the k_x-axis at $t^* = 0$ (the initial isotropic state) and $t^* \approx 2$ (time of peak small-scale anisotropy). Large-scale forcing causes the initially uniform angular distributions to become highly concentrated around $\gamma_a \sim \gamma_b \sim \pm 90°$. That is, the Fourier velocities of the most energetic modes surrounding the k_x-axis are forced by the large–small scale distant triadic interactions to align approximately with k_z.

In a similar fashion, we find that the complex velocities of the Fourier modes in the highly energetic region surrounding the k_y-axis are also forced to align with the k_z-direction so that the entire high-wavenumber region is dominated by z-component velocity fluctuations. We conclude that the spectral consequences of distant interactions

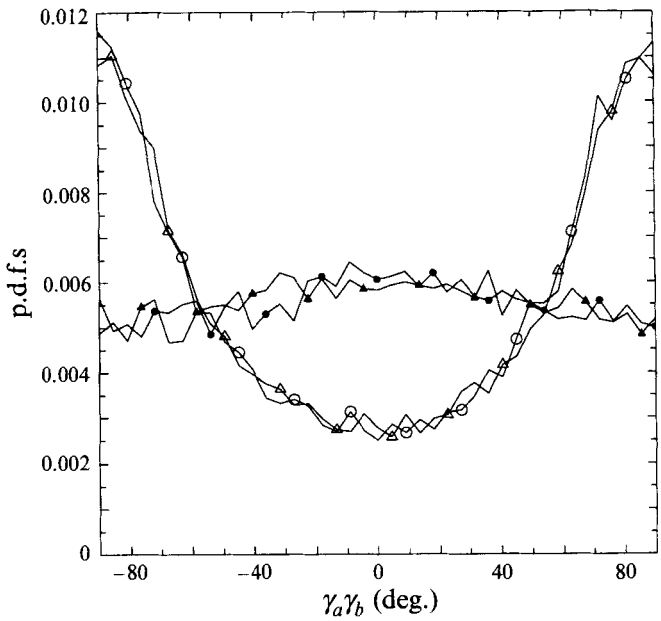

FIGURE 12. Probability density functions (p.d.f.s) of the azimuthal angles γ_a and γ_b of the real (triangles) and imaginary parts (circles) of the complex Fourier velocity around the k_x-axis in the (k_x, k_z)-plane (see figure 11), restricted to Fourier modes within the region $40 \leqslant k \leqslant 50$, $50° \leqslant \theta < 130°$ and $0° \leqslant |\phi| < 20°$ around the k_y-axis (see figure 10). Closed symbols are for the initial isotropic state; open symbols are for the turbulence at peak small-scale anisotropy, $t^* = 1.915$.

in this forced flow are not only to redistribute energy into certain dominant regions of Fourier space, but also to force certain phase couplings to exist among the Fourier modes within these energetic regions. While the alignment of the real and imaginary parts of the Fourier coefficients was predicted by the asymptotic form of the triadic equations for distant interactions (§3.2), the specific alignment of $\hat{\boldsymbol{u}}(\boldsymbol{k})$ with k_z is not obvious from (5) and (6). We show in the next section that these spectral processes of energy redistribution and forced phase coupling in wavenumber space are dynamically equivalent in physical space to the formation of small-scale vortices with dominant vorticity aligned in the x- and y-directions.

7.3. *Redistribution of small-scale vorticity*

It was shown in figure 8 that at peak small-scale anisotropy, high-wavenumber vorticity is primarily in the ω_1 and ω_2 components. It is now clear, from the discussion above, why. The vorticity in a Fourier mode is given by $\hat{\boldsymbol{\omega}}(\boldsymbol{k}) = -\mathrm{i}\boldsymbol{k} \times \hat{\boldsymbol{u}}(\boldsymbol{k})$. Thus, because $\hat{\boldsymbol{u}}(\boldsymbol{k})$ is aligned with k_z at the small scales, those most energetic modes surrounding the k_x-axis contribute primarily to vorticity in the y-direction, whereas those most energetic modes surrounding the k_y-axis contribute primarily to x-vorticity. This is indeed the case, as shown in figure 13(a, b), where the distributions of $V_{11}(\boldsymbol{k}) \equiv \hat{\omega}_1(\boldsymbol{k})\,\hat{\omega}_1^*(\boldsymbol{k})$ and $V_{22}(\boldsymbol{k}) \equiv \hat{\omega}_2(\boldsymbol{k})\,\hat{\omega}_2^*(\boldsymbol{k})$ are given in the high-wavenumber shell $40 \leqslant k < 50$. Note that the energetic modes near the k_y-axis ($\theta = 90°, \phi = \pm 90°$) contribute primarily to x-vorticity, whereas energetic modes near the k_x-axis ($\theta = 90°, \phi = 0$) contribute primarily to y-vorticity. Both groups of modes are strongly associated with spanwise energy.

The considerations above show that the anisotropic large-scale forcing leads to a small-scale structure dominated by separate localized regions of concentrated energy

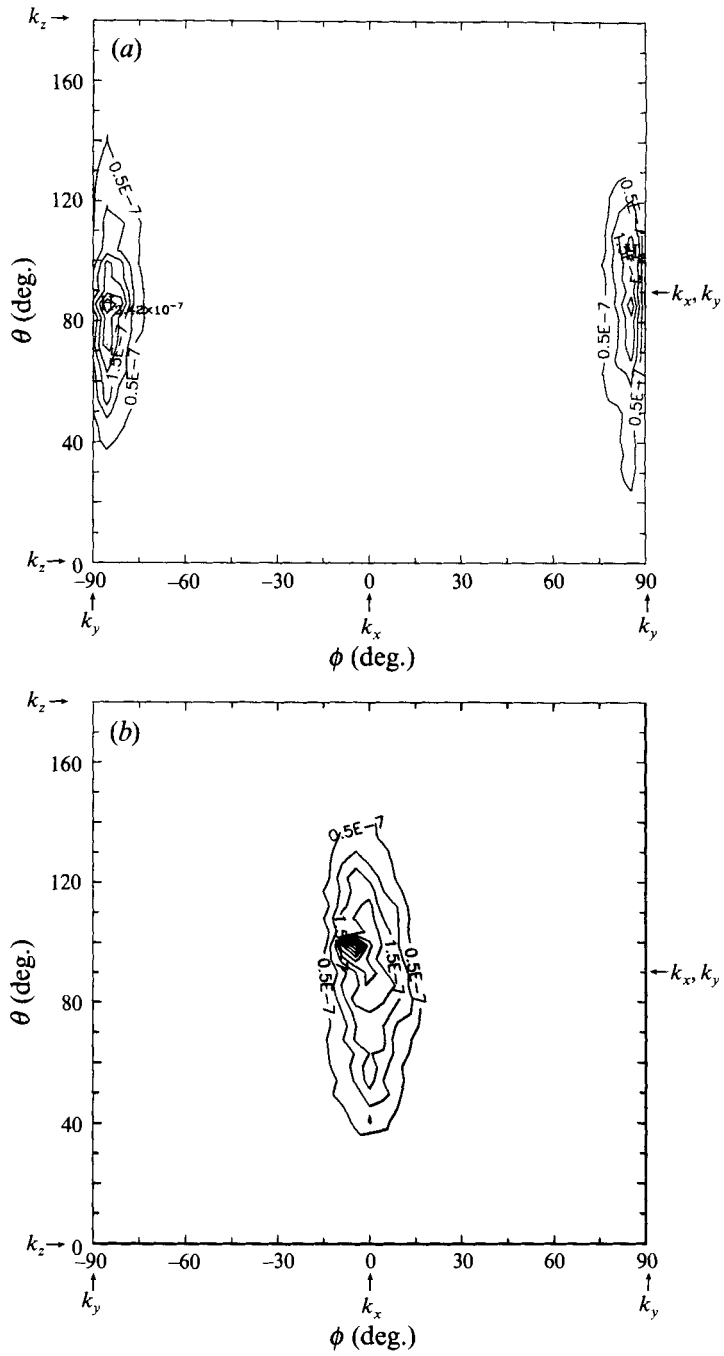

FIGURE 13. Isocontours of the spectral distributions of (*a*) ω_x^2 and (*b*) ω_y^2 in the region $40 \leqslant k \leqslant 50$ for forced turbulence at peak small-scale anisotropy, $t^* = 1.915$. The spherical coordinates are defined in figure 11.

and vorticity in Fourier space, one region associated with x-vorticity and the other with y-vorticity. We shall find in §8 that in physical space the x-vorticity modes (aligned with k_y) and the y-vorticity modes (aligned with k_z) are separately associated with rectilinear vortices in the x- and y-directions, respectively.

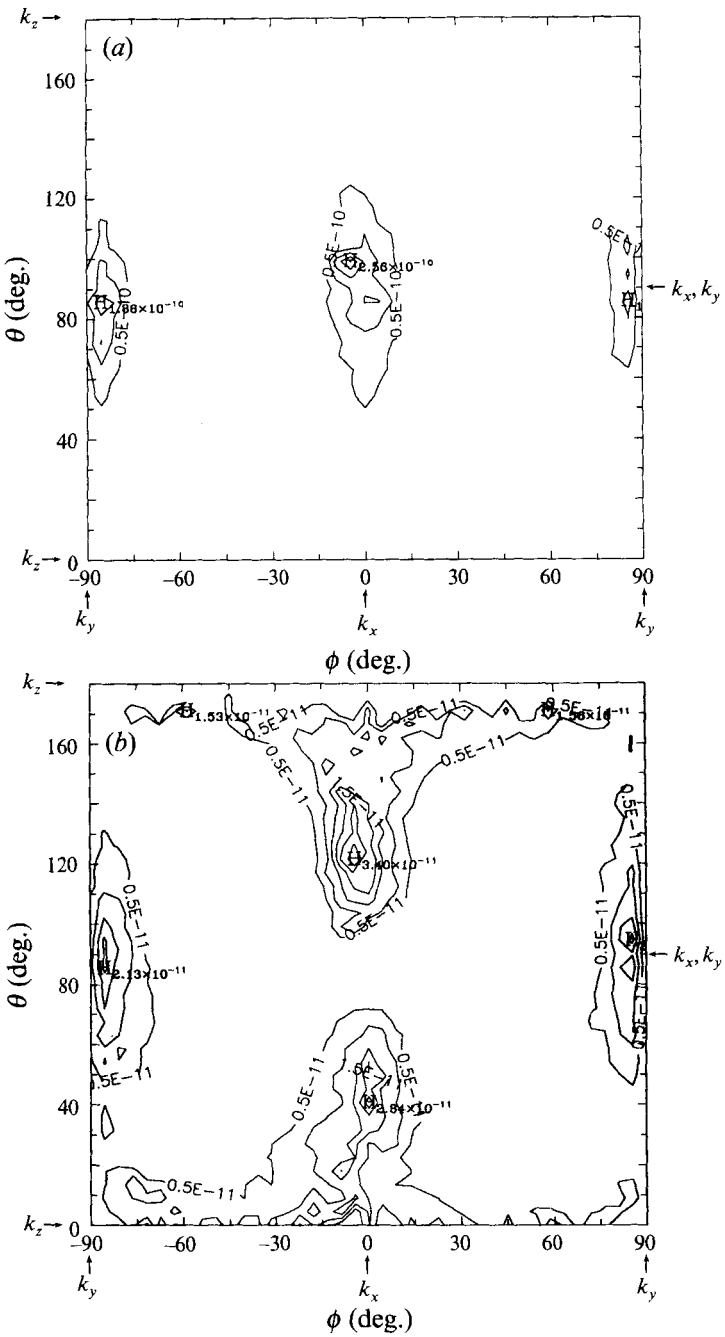

FIGURE 14. Isocontours of the spectral distributions of component turbulent kinetic energy within the high-wavenumber shell $40 \leqslant k < 50$ at peak small-scale anisotropy, $t^* = 1.915$. (*a*) $E_{33}(\boldsymbol{k})$, the *z*-component; (*b*) $E_{11}(\boldsymbol{k})$, the *x*-component. The spherical coordinates are defined in figure 11.

The helicity of a Fourier mode is given by (Polifke & Shiltman 1989)

$$H(\boldsymbol{k}) = 2\boldsymbol{k}\cdot[\boldsymbol{a}(\boldsymbol{k}) \times \boldsymbol{b}(\boldsymbol{k})], \tag{34}$$

where $\boldsymbol{a}(\boldsymbol{k})$ and $\boldsymbol{b}(\boldsymbol{k})$ are the real and imaginary parts of $\hat{\boldsymbol{u}}(\boldsymbol{k})$. Because large-scale forcing causes $\boldsymbol{a}(\boldsymbol{k})$ and $\boldsymbol{b}(\boldsymbol{k})$ to align in the small-scale modes surrounding the k_x- and

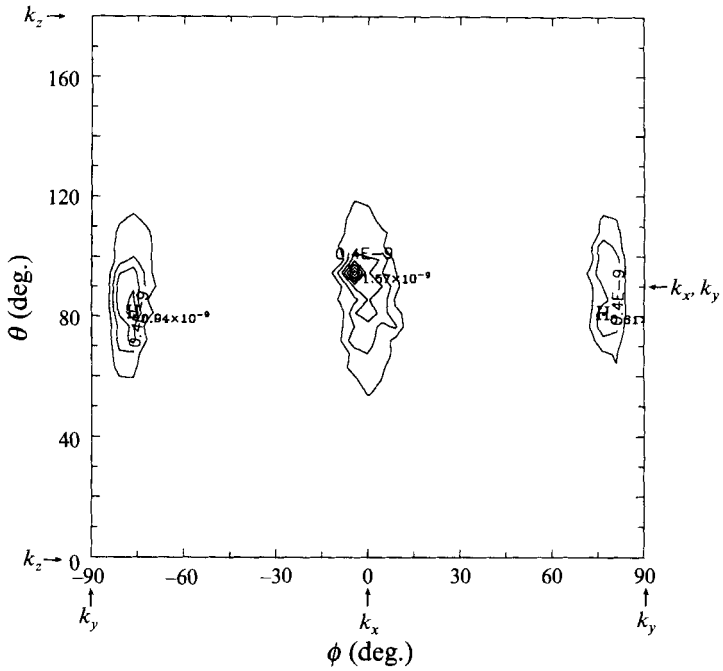

FIGURE 15. Isocontours of the rate of spanwise energy transfer $T_{33}(k)$ within the high-wavenumber shell $40 \leqslant k < 50$ at peak small-scale anisotropy, $t^* = 1.915$, considering only contributions from the forced triads.

k_y-axes, those dominant modes contributing to the small-scale vorticity and velocity fields are non-helical, implying that the x-vortices carry mostly y- and z-velocity, while the y-vortices carry mostly x- and z-velocity. In this way, the spanwise (z) velocity becomes the most energetic component.

7.4. *Redistribution of small-scale component energy*

Evolution of the energy spectrum is determined by nonlinear energy transfer and viscous dissipation (equations (24) and (25)). We have shown previously (YB), by considering the banded energy transfer functions $T_{\alpha\alpha}(k\,|\,p, q)$ (equations (25) and (26)), that a highly non-local and distant triadic group involving the directly forced modes is the source of small-scale anisotropy development. The dominance of distant triads is especially pronounced for energy transfer $T_{33}(k)$ into the spanwise component. In the shell $42.5 \leqslant k < 47.5$, for example, 73.3% of $T_{33}(k)$ at peak small-scale anisotropy is contributed by triads in which one leg is within $2 \leqslant k < 4$ and the third leg is within $32 \leqslant k < 64$.

In §3.3 we argued, based on the asymptotic form of $T_{\alpha\alpha}(\boldsymbol{k})$ (equation (13)), that coherent forcing through $\pm \boldsymbol{k}_F^{(n)}$ induces a greater level of energy transfer in the z-direction as compared with x and y. More specifically we argued that those energy-dominant small-scale modes surrounding the k_y-axis would transfer energy into E_{11} and E_{33} whereas those surrounding k_x transfer energy into E_{22} and E_{33}. The net effect of these large–small scale interactions on $E_{11}(\boldsymbol{k})$ and $E_{33}(\boldsymbol{k})$ at the small scales is shown after forcing in figure 14. It is clear by comparing figure 14(a) with figure 10 that both total kinetic energy $E_{ii}(\boldsymbol{k})$ and the z-component $E_{33}(\boldsymbol{k})$ are highly concentrated near the k_x- and k_y-axes and that, as predicted, most of the turbulent kinetic energy in these regions is in the z-component.

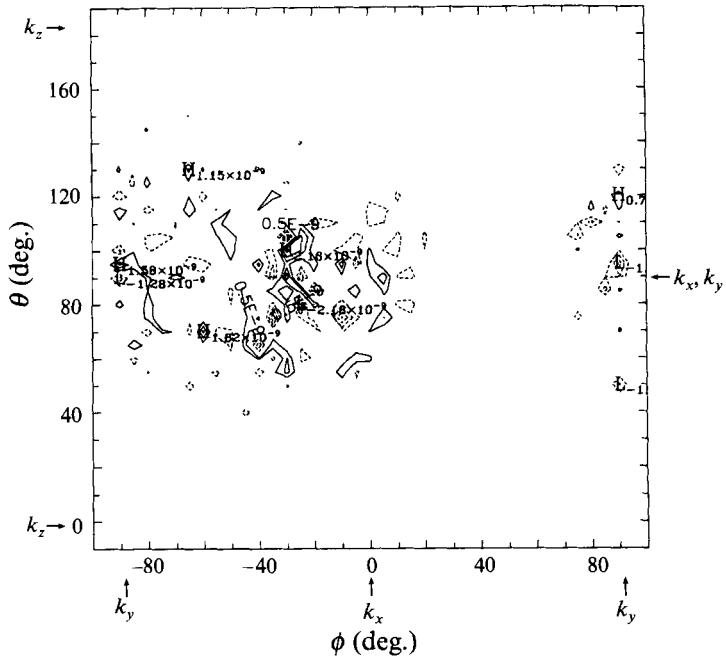

FIGURE 16. Isocontours of the rate of spanwise energy transfer $T_{33}(k)$ within the high-wavenumber shell $40 \leqslant k < 50$ immediately after the impulsive addition of energy to $\pm \boldsymbol{k}_F^{(1)}$, considering only contributions from the forced triads. Solid and dashed contours are for positive and negative levels, respectively. Note the depletion of energy in the direction of $\boldsymbol{k}_F^{(1)}$ ($\theta = 90°, \phi = 45°$).

Figure 14(*b*) shows that $E_{11}(\boldsymbol{k})$ is at least one order of magnitude smaller than $E_{33}(\boldsymbol{k})$ and, as expected, contains contributions from high-wavenumber modes surrounding the k_y-axis (as well as contributions surrounding the k_x, k_z-plane). Similarly, $E_{22}(\boldsymbol{k}) \ll E_{33}(\boldsymbol{k})$ and contains contributions from modes surrounding the k_x-axis.

Figure 15 shows the *rate of energy transfer* $T_{33}(\boldsymbol{k})$ over the high-wavenumber shells and at the same instant as figure 14, including only contributions from triads which contained a forced mode as one leg. Figure 15 shows that after continual forcing over 2 eddy turnover times, both the energy and the transfer of energy into the z-direction by the forced triads is concentrated within those energetically dominant modes surrounding the k_x- and k_y-axes.

The energy transfer in figure 15 represents the cumulative effect of continual forcing beginning with a uniform isotropic initial distribution of energy and phase in the high-wavenumber shell. To demonstrate that this cumulative effect is due to direct small-scale coupling with the large-scale coherently forced modes, consider the applications of an impulsive increase in energy in one pair of forced modes $\pm \boldsymbol{k}_F^{(1)}$. Figure 16 shows isocontours of $T_{33}(\boldsymbol{k})$ just after impulsive forcing in the same high-wavenumber shell as figure 15. (Note that, by continuity, modes in the k_z-direction cannot exchange energy with the z-direction, so T_{33} must be small there.) What is important is the reduction in energy transfer in the direction of the large-scale impulsively forced modes $\boldsymbol{k}_F^{(1)}$ ($\theta = 90°, \phi = 45°$). Similarly, had we impulsively forced $\pm \boldsymbol{k}_F^{(2)}$ we would have found a reduction in T_{33} in the direction of $\boldsymbol{k}_F^{(2)}$ ($\theta = 90°, \phi = -45°$). However, because each forced mode transfers energy in the direction of the other forced mode, when both $\pm \boldsymbol{k}_F^{(1)}$ and $\pm \boldsymbol{k}_F^{(2)}$ are impulsively forced simultaneously, as shown in figure 17, a lesser but still perceptible reduction in $T_{33}(\boldsymbol{k})$ exists in the direction of all forced modes

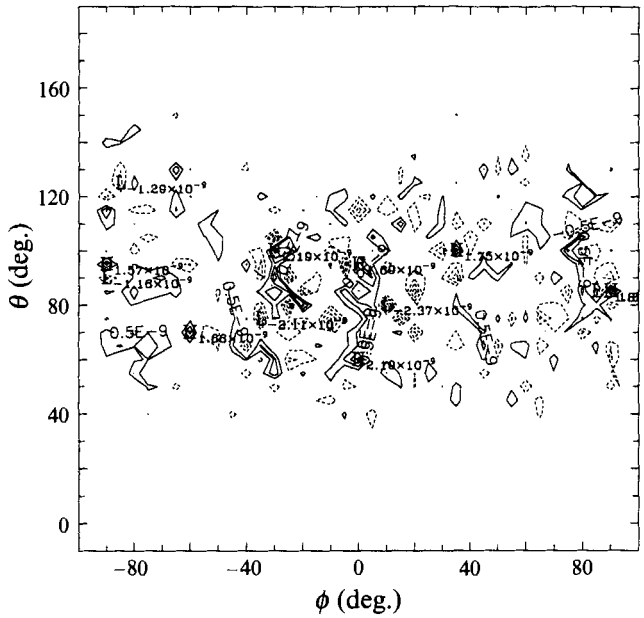

FIGURE 17. Isocontours of the rate of spanwise energy transfer $T_{33}(k)$ within the high-wavenumber shell $40 \leqslant k < 50$ immediately after the impulsive addition of energy to $\pm \boldsymbol{k}_F^{(1)}$ and $\pm \boldsymbol{k}_F^{(2)}$. Compare with figure 16. Note the relative depletion of energy in the direction of forced modes $\boldsymbol{k}_F^{(n)}$ ($\theta = 90°$, $\phi = \pm 45°$).

($\theta = 90°, \phi = \pm 45°$). During continuous forcing, the continual reduction of energy transfer in the $\pm \boldsymbol{k}_F^{(n)}$ direction leads, over time, to a significant depletion of E_{33} and correspondingly greater reductions in T_{33} in the direction of the forced large-scale modes.

It is apparent that the creation of small-scale anisotropy through distant triadic couplings will be sensitive to the degree of anisotropy in the large-scale forced modes and to the intensity of forcing, and will be time dependent. As discussed in §§3.4 and 10, anisotropy at the small scales also depends on the changing interplay between the distant triadic group and the local-to-non-local energy cascading interactions.

8. The physical-space view of small-scale restructuring by large–small scale non-cascading interactions

YB showed that the development of anisotropy at the small scales due to anisotropic coherent forcing at low wavenumbers is a direct consequence of the most non-local and distant triadic interactions in the simulation. In the last section we showed that this small-scale anisotropy is due to a restructuring of Fourier space from the low-wavenumber forcing which can be predicted, to a large extent, from the equations describing individual members of the distant triadic group. In addition we found that the small scales evolve from forcing to a vorticity field dominated by two components in vorticity, ω_x and ω_y, and one component in velocity, w. An important observation is that each vorticity component is localized in Fourier-space; ω_x and ω_y are directly associated with Fourier modes surrounding the k_y- and k_x-axes, respectively, as shown in figure 13. In this section we describe the corresponding physical-space structure at peak anisotropy, and in §9 we develop the physical-space dynamical interpretation of distant triadic interactions leading to small-scale anisotropy.

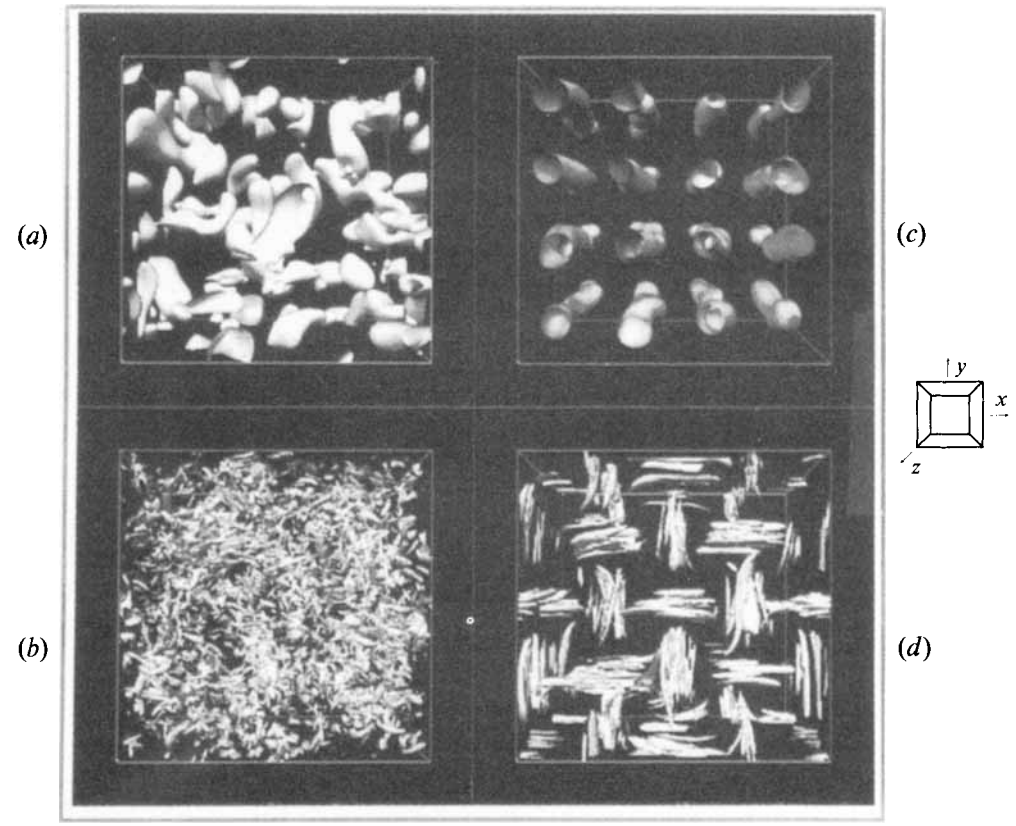

FIGURE 18. Three-dimensional isosurfaces of enstrophy in physical space from the wavelet transformed vorticity field before forcing and after forcing at peak small-scale anisotropy, $t^* = 1.915$. Each vorticity component is first passed through the three-dimensional Mexican-hat wavelet filter with peak at $k = k_a$ and then squared and summed. (*a*) Isotropic state at the large scales ($k_a = 3$); (*b*) isotropic state at the small scales ($k_a = 40$); (*c*) forced turbulence at peak small-scale anisotropy, $t^* = 1.915$, at the large scales ($k_a = 3$); (*d*) forced turbulence at $t^* = 1.915$ at the small scales ($k_a = 40$). The isosurface levels for the left and right figures are 1.5 r.m.s. and 2.5 r.m.s. above the mean values of the wavelet transformed enstrophy fields, respectively.

We obtain visual representations of the enstrophy field by applying the Mexican-hat wavelet transform as a spectral filter to the vorticity vector field $\boldsymbol{\omega}(\boldsymbol{x})$, and then forming the scale-dependent filtered enstrophy field $\Phi^2(\boldsymbol{\xi}, a)$, as described in §4 (equations (29)–(32)). As discussed in §4, the wavelet filter has the advantage of a clear physical-space interpretation in which scale-dependent locality surrounding $\boldsymbol{\xi}$ in physical space corresponds to a scale-dependent local filtering around $\boldsymbol{k}_a$ in Fourier space. The magnitude of $\boldsymbol{k}_a$ is inversely proportional to the wavelet scale, a. Because the Mexican-hat wavelet is spherically symmetric in physical and Fourier space, $\boldsymbol{k}_a$ becomes scalar k_a, and applying the wavelet transform is qualitatively similar to filtering Fourier modes dominantly from spectral shells centred on $k = k_a$ with shell thickness Δk_a, where k_a and Δk_a both scale on $1/a$ (see Brasseur & Wang 1992). The result is a spherically filtered signal around $k_a \sim 1/a$ which corresponds in physical space to the isotropic selection of structures with dominant physical-space scale a. Because the wavelet filter is continuous in Fourier space covering a range of scales automatically adjusted to the physical-space scale a, the Mexican-hat wavelet transformed signal is generally a more realistic visual representation of physical-space structure than a band-pass-filtered signal.

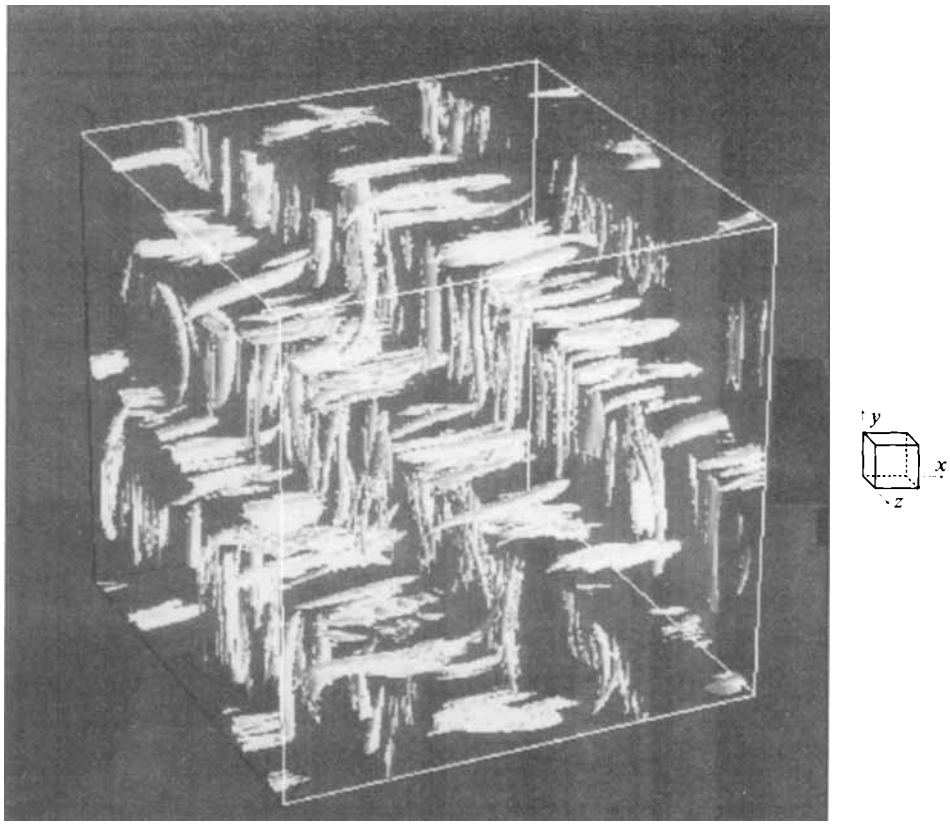

FIGURE 19. The same field as in figure 18(*d*) from a different angle: three-dimensional isosurfaces of enstrophy from the Mexican-hat wavelet transformed vorticity field in physical space at peak small-scale ansotropy, $I^* = 1.915$, at the small scales ($k_a = 40$).

To distinguish the large-scale forced modes from the small scales, the wavelet filter is aligned with its peak at $k_a = 3$ ('large scale') and $k_a = 40$ ('small scale'). At large values of k_a the wavelet filter is very broad and the small-scale filter includes a small amount of information from large scales. Nevertheless, the filters do a good job of separating scales of motion and we shall see that the large- and small-scale structures are very different after forcing. Figure 18 shows three-dimensional enstrophy isosurfaces from the wavelet filtered vorticity field before forcing (*a*, *b*) and after forcing (*c*, *d*). Large scales are given by (*a*) and (*c*), and small scales by (*b*) and (*d*). Before forcing both the large- and small-scale enstrophy fields are statistically isotropic, there being equal probability of statistically similar structures in all directions. The small-scale vorticity field, in particular, consists of highly localized vortical spikes in elongated regions. It has been shown by a number of workers that, in moderate Reynolds number isotropic turbulence, the more intense localized regions are tube-like with vorticity aligned in the axial direction along the vortex tubes (She, Jackson & Orszag 1990; Vincent & Meneguzzi 1991; Jimenez *et al.* 1993; Lin 1993).

After forcing for nearly 2 eddy turnover times, the large-scale structure consists of elongated vortex tubes aligned in z (figure 18*c*), corresponding closely to the rectilinear forced vortices shown in figure 3. The large-scale vortices display variations in z associated with the non-forced low-wavenumber modes. At the small scales (figure 18*d*),

multiple slender tube-like enstrophy structures are observed. These structures are primarily oriented in x or y, and have typical lengths approximately equal to the separation distance between the cores of adjacent forcing vortices, which, in wavenumber space, are related to the length of the four forced Fourier modes. Thus, there is a relationship between the lengths of the vortex tubes and the topology of the large-scale forcing, information passed on through the distant triadic group. Figure 19 shows the structures in figure 18(d) looking from another angle, making it clear that the small-scale enstrophy structures are elongated in the x- and y-directions, lying roughly side by side in the z-direction. No z-oriented vortices are created by the two-dimensional large-scale forcing.

Figures 18 and 19 indicate that the distant triadic couplings between the large-scale forced modes and the small-scale vortical modes have led to the development of organized small-scale vortical structures in physical space with highly anisotropic preferential directions. It might be suspected from these figures that the vortical structures aligned with x and y are vortex tubes with axial vorticity in the x- and y-directions, respectively. This is, in fact, the case, as shown in figure 20(a, b). Figure 20(a) shows isosurfaces of ω_x^2 from the small-scale wavelet transformed vorticity field, while figure 20(b) shows isosurfaces of ω_y^2. It is clear from these figures that vertically and horizontally aligned vortex structures are vortex tubes with appropriately signed vorticity.

Particularly interesting is that the vertically and horizontally aligned vortex tubes, created through distant triadic couplings with the large-scale forcing field, are separately associated with localized regions in high-wavenumber Fourier-space. Recall from the isosurfaces of spectral enstrophy in figure 9 that small-scale vorticity is concentrated in regions surrounding the k_x- and k_y-axes in high-wavenumber Fourier space. From figure 13 we learned that the x- and y-components of vorticity are separately concentrated within ellipsoidal regions surrounding the k_y- and k_x-axes, respectively, suggesting that the Fourier modes might carry the information necessary to reconstruct the x- and y-vortices in figure 18(d). This is in fact the case, as shown in figure 20(c, d). Here, rather than filtering the signal within spherically symmetric spectral *shells*, we filter locally from within *spheres* centred on pairs of equal and opposite high-wavenumber wavevectors $\pm \boldsymbol{k}_a$, where $\boldsymbol{k}_a$ lies either on the k_x-axis or the k_y-axis. More precisely, 'Morlet' wavelet filters (see Brasseur & Wang 1992; Wang *et al.* 1994) are used to extract Fourier space within pairs of spherical Gaussian envelopes centred on $\pm \boldsymbol{k}_a$, where $\boldsymbol{k}_a = 30\hat{\boldsymbol{e}}_x$ or $\boldsymbol{k}_a = 30\hat{\boldsymbol{e}}_y$. The corresponding physical-space enstrophy fields associated with the locally filtered high-wavenumber modes surrounding the k_x or k_y axes are shown in figures 20(c) and 20(d), respectively. Figure 20(c) shows that the x-vortices are localized in Fourier space around the k_y-axis at high wavenumbers; figure 20(d) shows that the y-vortices are localized around the k_x-axis. We learned from figure 12 that in each of these localized regions the Fourier coefficients is aligned in the k_z-direction, thus providing the appropriate sign of vorticity within the x- and y-oriented vortices. These structural relationships are a direct consequence of the marginally distant triadic interactions.

From these results, it is clear that the spectral regions of concentrated ω_x and ω_y shown in figure 13(a, b) individually describe subsets of directionally dependent vortex tubes in physical space. Note that those ellipsoids in figure 13 separately containing the small-scale x- and y-vorticity field are greatly elongated in the k_z-direction. Fourier modes in these regions with a significant k_z component are necessary to characterize spanwise gradients of vorticity in the x and y vortex tubes, as is apparent in figures 18(d) and 19.

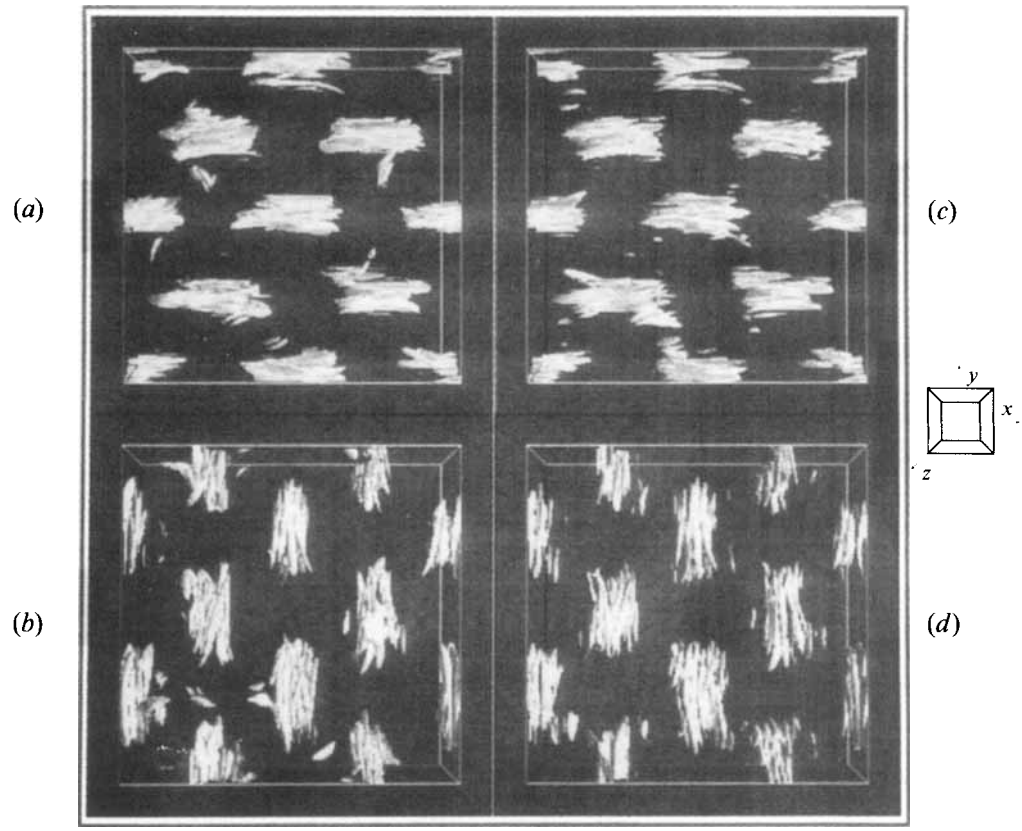

FIGURE 20. There-dimensional isosurfaces of enstrophy from the wavelet transformed vorticity field at peak small-scale anisotropy, $t^* = 1.915$, at the small scales. The isosurface levels are 2.5 r.m.s. above the mean value of the wavelet transformed enstrophy field. (*a*), (*b*) Isosurfaces of ω_x^2 and ω_y^2 at the small scales with the vorticity field components passed through a Mexican-hat wavelet filter with peak at $k_a = 40$. (*c*), (*d*) Isosurfaces of Morlet-wavelet filtered enstrophy fields. The Morlet wavelet filters from localized spherical regions in Fourier space centred on the two symmetrically located points $\pm \boldsymbol{k}_a$, where $\boldsymbol{k}_a = \boldsymbol{k}_0/a$; here a is the wavelet scaling parameter (see equation (29)) and $\boldsymbol{k}_0$ is a wavevector defined in the Morlet wavelet filter, $\hat{g}(\boldsymbol{k}) = \frac{1}{2}\pi^{3/2}[e^{-(k-k_0)^2/4} + e^{-(k+k_0)^2/4}]$. Only the real part of the wavelet filter is applied. In (*c*) $\boldsymbol{k}_a = [0, 30, 0]$, localizing the filter around the high-wavenumber regions of the k_y-axis. In (*d*) $\boldsymbol{k}_a = [30, 0, 0]$, selecting modes from the high-wavenumber regions of the k_x-axis. By comparing (*c*) and (*a*), and (*d*) and (*b*) we see that the high-wavenumber Fourier modes in local regions surrounding the k_y- and k_x-axes separately create the vortex tubes in the x- and y-directions, respectively.

9. Dynamics of large–small scale non-cascading interactions in the physical-space view

We have learned that the distant triadic group leads to a redistribution of energy and phase in high-wavenumber Fourier space which in physical space corresponds to the creation of strongly aligned small-scale vortex tubes. Whereas the dynamical process of direct large–small scale interactions has been discussed in terms of triadic interactions in the spectral view, we focus in this section on the corresponding physical-space description.

Qualitatively it is not difficult to understand the restructuring of the small-scale enstrophy field as the advection and distortion of small-scale vorticity by the large-scale energy-dominated eddies. To see this, consider again the large-scale velocity field induced by the forced modes shown in figure 3. The corresponding large-scale strain-

rate field at the time of maximum anisotropy ($t^* = 2$) is shown in figure 21. In this figure the strain-rate component s_{11} has been filtered with a low-wavenumber band-pass filter covering the range $\{0 < k < 6\}$ (as for equation (27) with $\hat{\boldsymbol{u}}$ replaced by s_{11}). Because s_{33} is zero in the forced modes, $s_{22} \approx -s_{11}$ within the forced band of scales. Note that the counter-rotating vortices established at the large scales create large elongational and compressional strain rates in the 'stagnation point' regions between the forced vortices. One might speculate, therefore, that the physical-space description of large-scale energy-dominated modes directly influencing small-scale vorticity-dominated modes within distant triadic interactions is essentially described by differential large-scale advection, rotation, and deformation of the small-scale vorticity field. Specifically, as the large-scale two-dimensional vortices are created by forcing, a velocity field is established which advects small-scale vorticity towards the high-strain regions between the forced vortices. As the vorticity accumulates it tends to align with the direction of principle elongational strain, which alternates among the forced 'stagnation points'. We showed in the previous section that the formation of these vortex tubes is in one-to-one correspondence with the redistribution of energy and phase in high-wavenumber Fourier space – which itself is the dynamical consequence of the distant triadic group applicable at infinite scale separation.

Although details are missing, we shall see that the explanation above qualitatively captures the essential physics of large–small scale interaction in the current experiment. To show this, consider the dynamic equation which describes the change in small-scale component enstrophy, filtered from the high-wavenumber spectral shell $\mathscr{H}$, $\langle(\omega_\alpha|\mathscr{H})^2\rangle$:

$$\frac{1}{2}\frac{\partial}{\partial t}\langle(\omega_\alpha|\mathscr{H})^2\rangle = -\left\langle(\omega_\alpha|\mathscr{H})\left(u_j\frac{\partial\omega_\alpha}{\partial x_j}|\mathscr{H}\right)\right\rangle + \langle(\omega_\alpha|\mathscr{H})(\omega_j s_{\alpha j}|\mathscr{H})\rangle$$
$$-\nu\left\langle\frac{\partial(\omega_\alpha|\mathscr{H})}{\partial x_j}\frac{\partial(\omega_\alpha|\mathscr{H})}{\partial x_j}\right\rangle, \tag{35}$$

where summation is only over Latin indices. Here we use the notation introduced in (28), where $(\omega_\alpha|\mathscr{H})$ is a band-pass-filtered vorticity component, the filter being within the same high-wavenumber band as in previous figures:

$$\mathscr{H} = \{40 \leqslant k < 50\}. \tag{36}$$

The terms on the right-hand side of (35) are advection, straining and dissipation of small-scale component vorticity, respectively. The change in total small-scale enstrophy is given by the sum of (35) over $\alpha = 1, 2, 3$.

As an example, to calculate the advection term we first multiply velocity and vorticity gradients in physical space, then transform the product to wavenumber space. Retaining only the contributions from Fourier modes inside the set $\mathscr{H}$, we then transform back to physical space and correlate the filtered product with the filtered vorticity.

Figure 22 shows the budget of the small-scale vorticity field during forcing, where curves A, B, C and D represent each term in (35) from left to right. The inset gives an expanded view within the period of small-scale anisotropy in $E_{ij}(k)$, the period from $t_1^* = 0.9$ to $t_3^* = 3.5$, as shown in figure 7. Peak small-scale anisotropy is near $t_2^* = 2$. Note that small-scale advection (B) and straining (C) increase as a result of large-scale forcing. However, the net increase in advection and straining is nearly balanced by a corresponding increase in viscous dissipation so that the rate of change of small-scale enstrophy (A) is nearly zero during the reorganization of the small scales into aligned

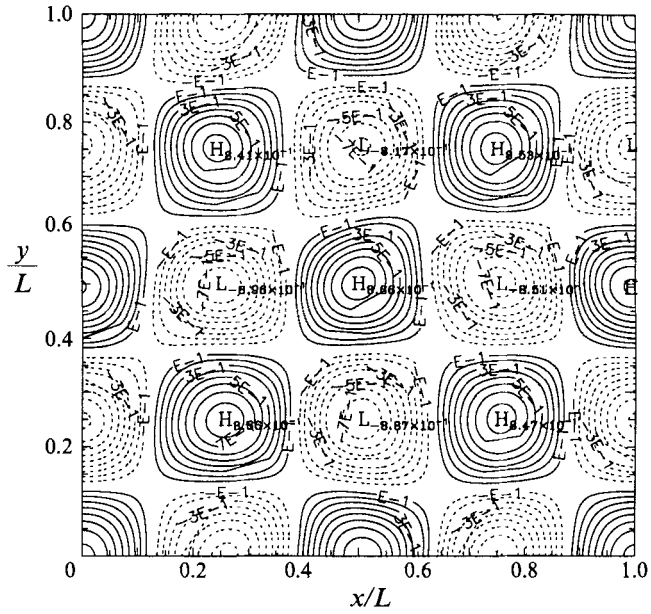

FIGURE 21. Isocontours of the large-scale strain-rate components s_{11} in the (x, y)-plane passed through the low-wavenumber band-pass filter $\mathscr{L} = \{\boldsymbol{k}: 0 < k < 6\}$ at peak small-scale anisotropy, $t^* = 1.915$, after averaging over the z-direction. Solid and dashed lines are positive and negative isocontours, respectively.

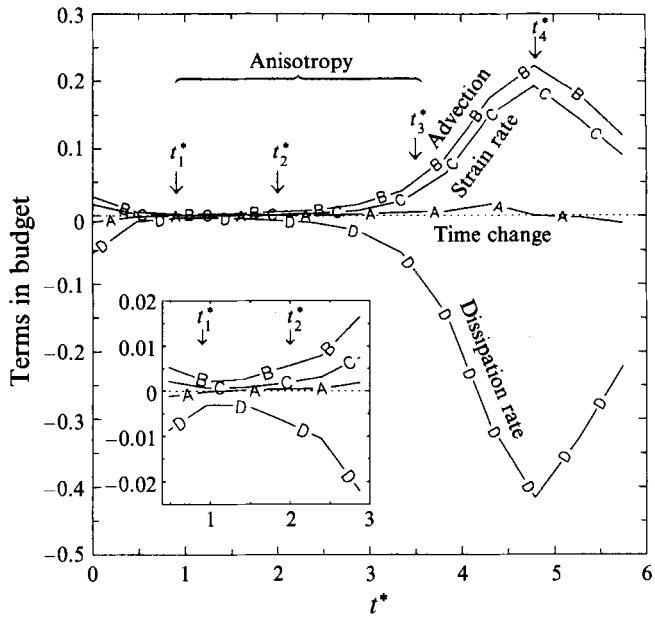

FIGURE 22. Temporal evolution of different terms of the budget of small-scale x-vorticity variance (equation (35), with $\alpha = 1$, where $\mathscr{H} = \{\boldsymbol{k}: 40 \leqslant k < 50\}$). The terms are: net rate of change $\partial/\partial t\langle(\omega_x|\mathscr{H})^2\rangle$ (A), advection (B), straining (C), and vorticity dissipation (D). The early-time evolution is shown magnified in the inset. t_1^* and t_3^* are the period of small-scale anisotropy in $E_{ij}(k)$ from figure 7. Peak small-scale anisotropy is at $t^* = 1.915$; $t_4^* = 4.8$ is the beginning of the second period of decay in figure 4.

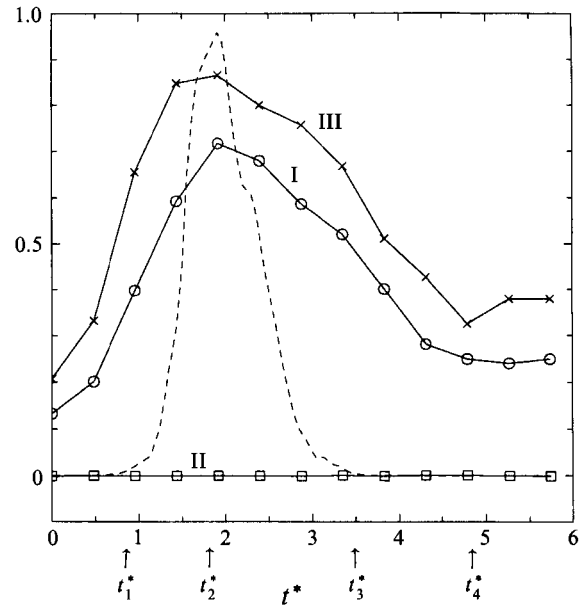

FIGURE 23. Comparison of the advection of small-scale component vorticity ω_x^2 by all the scales $[\mathscr{M}:\mathscr{H}]$ with (I) small-scale advection by large scales on small scale ω_x^2 $[\mathscr{L}:\mathscr{H}]$, (II) small-scale advection by the small scales on small scale ω_x^2 $[\mathscr{H}:\mathscr{H}]$, and (III) advection by the large scales on the subset of Fourier modes within $\mathscr{H}$ in which most of ω_x^2 lies, $[\mathscr{L}:\mathscr{H}_x]$. More precisely, the three solid curves give the ratios, (I) $[\mathscr{L}:\mathscr{H}]/[\mathscr{M}:\mathscr{H}]$, (II) $[\mathscr{H}:\mathscr{H}]/[\mathscr{M}:\mathscr{H}]$, (III) $[\mathscr{L}:\mathscr{H}_x]/[\mathscr{L}:\mathscr{H}]$. The dashed curve shows the anisotropy invariant $\mathrm{III}_A(k)$ against t^* for the highest-wavenumber shell (curve K in figure 7). t_1^*, t_2^*, t_3^*, and t_4^* are defined in figure 22. See §9 for discussion.

vortex tubes, and remains small relative to the other terms in (35). Note that significant enstrophy production begins during the return-towards-isotropy period ($t^* > t_2^*$), and changes sign at the initiation of the second equilibrium state ($t^* \geqslant t_4^*$, where $t_4^* = 4.8$ from figure 4).

It is clear from figure 22 that strain rate and advection of small-scale vorticity increase as a consequence of large-scale forcing. It is not clear, however, which scales are primarily responsible for small-scale advection and strain. To discover this, we further separate the advection and straining terms in (35) into separate contributions from large and small scales. This is done by pre-filtering $\boldsymbol{u}$ and s_{ij} in wavenumber space through a filter $\mathscr{L}$ or through filter $\mathscr{H}$. When pre-filtered through $\mathscr{L}$, the advection and straining terms become

$$\text{advection:} \quad -\left\langle (\omega_\alpha \,|\, \mathscr{H}) \left[\left((u_j \,|\, \mathscr{L}) \frac{\partial \omega_\alpha}{\mathrm{d}x_j} \right) | \, \mathscr{H} \right] \right\rangle, \tag{37}$$

$$\text{straining:} \quad -\langle (\omega_\alpha \,|\, \mathscr{H}) [(\omega_j (s_{\alpha j} \,|\, \mathscr{L})) \,|\, \mathscr{H}] \rangle. \tag{38}$$

The terms in (37) and (38) represent the advection of mean-square small-scale vorticity by the large-scale velocity field, and amplification or attenuation of mean-square small-scale vorticity by the large-scale strain rate. Similarly, advection and straining of mean-square small-scale vorticity by the small-scale velocity field is given by replacing $\mathscr{L}$ with $\mathscr{H}$. Expressions (37) and (38) are additive over disjoint choices of the set $\mathscr{L}$ and reduce to the forms in (35) if $\mathscr{L}$ is taken to be the set $\mathscr{M}$ of all Fourier modes. In what follows, the low-wavenumber shell $\mathscr{L}$ is defined to be

$$\mathscr{L} = \{0 < k < 6\}. \tag{39}$$

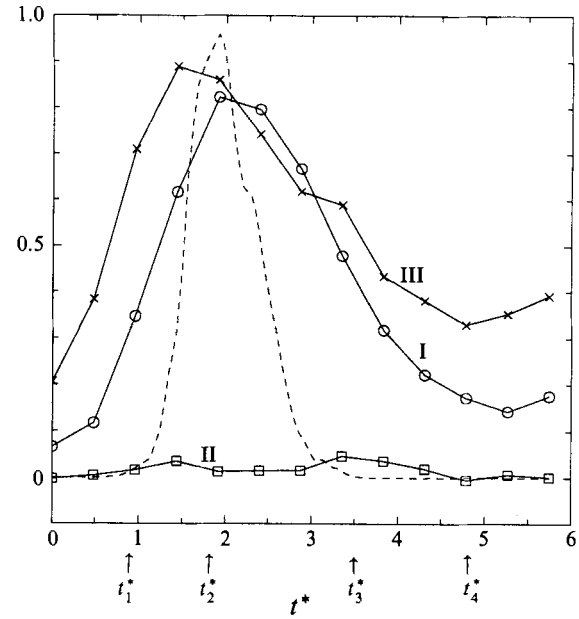

FIGURE 24. The same as figure 23 except that we consider straining of small-scale ω_x^2 rather than advection.

In figures 23 and 24 the relative contribution to the advection and straining, respectively, of small-scale component vorticity, ω_x^2, are compared:

curve I

Small-scale advection and straining by large scales on small scale ω_x^2, $[\mathscr{L}:\mathscr{H}]$, given by the terms in (37) and (38) with $\alpha = 1$ are compared with advection and straining from all scales, $[\mathscr{M}:\mathscr{H}]$, given by (35) with $\alpha = 1$.

curve II

Small-scale advection and straining by the small scales on small scale ω_x^2, $[\mathscr{H}:\mathscr{H}]$, given by replacing $\mathscr{L}$ in (37) and (38) with $\mathscr{H}$ are compared with advection and straining from all scales, $[\mathscr{M}:\mathscr{H}]$, given by (35) with $\alpha = 1$.

curve III

Advection and straining by the large scales on that subset of Fourier modes within Curves $\mathscr{H}$ containing most of ω_x^2, $[\mathscr{L}:\mathscr{H}_x]$, given by replacing $\mathscr{H}$ in (37) and (38) with the filter $\mathscr{H}_x$, are compared with advection and straining by the large scales on the small scales given by all Fourier modes in the shell $40 \leqslant k < 50$, $[\mathscr{L}:\mathscr{H}]$. $\mathscr{H}_x$ covers just those modes surrounding the k_y-axis in which ω_x^2 is concentrated as given by figure 13(*a*):

$$\mathscr{H}_x = \{40 \leqslant k < 50, 70° < |\phi| < 90°, 50° < \theta < 130°\}. \tag{40}$$

I, II, and III in figures 23 (advection) and 24 (straining) show the ratios $[\mathscr{L}:\mathscr{H}]/[\mathscr{M}:\mathscr{H}]$, $[\mathscr{H}:\mathscr{H}]/[\mathscr{M}:\mathscr{H}]$, and $[\mathscr{L}:\mathscr{H}_x]/[\mathscr{L}:\mathscr{H}]$, respectively, from the time of forcing.

Two features are immediately apparent from figures 23 and 24: (i) both advection and straining of the small scales by the large scales increase during the development of small-scale anisotropy to represent, by far, the largest contribution to total small-scale

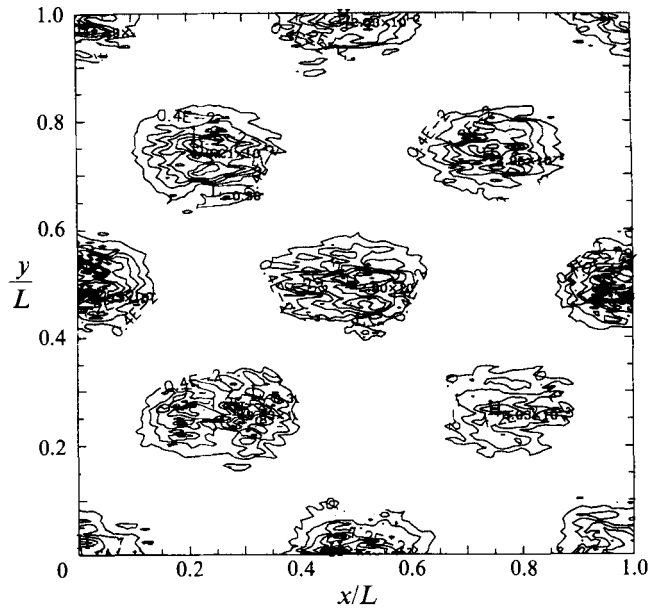

FIGURE 25. Isocontours of the advective effect in the (x, y)-plane on small-scale ω_x^2 due to the large-scale velocity field, after averaging over the z-direction. The contoured quantity is given by expression (37), with $\alpha = 1$, $\mathscr{L} = \{k: 0 < k < 6\}$ and $\mathscr{H} = \{k: 40 \leqslant k < 50\}$. Data are at peak small-scale anisotropy, $t^* = 1.915$, when the advective action is localized in regions of high small-scale ω_x^2 (compare with figure 20*a*, *c*). Similarly, small-scale straining by large scales is localized in the same regions.

advection and straining, and (ii) the local contribution to small-scale advection and straining from neighbouring small scales is negligible during forcing. Fully 72% of small-scale advection and 82% of small-scale straining comes from direct large–small scale interactions at the time of peak small-scale anisotropy (t_2^*). Even during the second equilibrium period ($t^* \gtrsim t_4^*$) 25% of small-scale advection and 18% of small-scale stretching comes from the large forced scales, about twice the 13% and 7% at the initiation of forcing.

The third observation to be made from figures 23 and 24 is that, as the small scales are restructured by large-scale forcing, most of the advection and stretching of small-scale ω_x^2 is associated with those Fourier modes in which ω_x^2 resides (set $\mathscr{H}_x$, above). As shown in figure 25, this corresponds, in physical space, to those localized regions in which the vortex tubes oriented in the x-direction reside (compare with figure 20), indicating that both advection and stretching of small-scale vorticity by the forced large scales are responsible for the creation and alignment of the vortex tubes in the stagnation-point regions between the large-scale forced vortices.

We conclude that, in this numerical experiment, the direct dynamical influence of large scales on small scales may be interpreted in physical space as the differential advection and straining of small-scale eddies by the large scales without significantly altering the net enstrophy (and energy) of the small scales. The Fourier spectral view adds a great deal more detail to these dynamical effects as distant triadic interactions between energy-dominated large scales and vorticity-dominated small scales. Specifically, while these long-range interactions alter the structure at the small scales at asymptotically large-scale separation, there is no direct transfer of turbulent kinetic energy between disparate scales. Because these long-range interactions exist at infinite

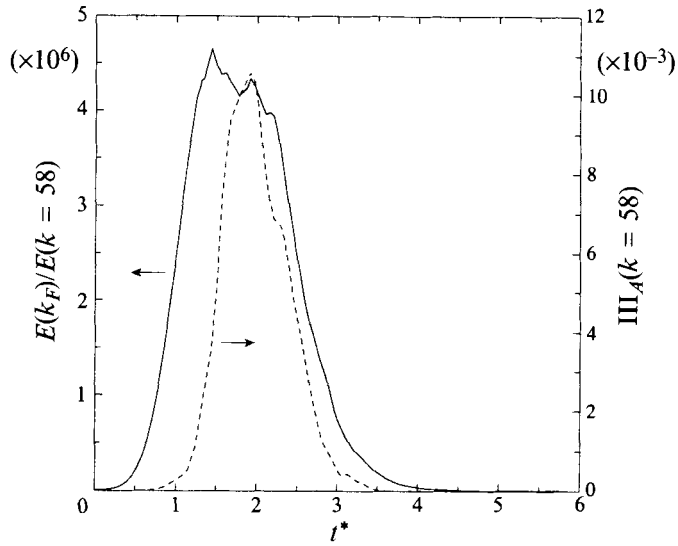

FIGURE 26. The ratio of energy in the unit-width shell surrounding the forced modes to that surrounding $k = 58$ against non-dimensional time t^*. The dashed line is the third invariant of $E_{ij}(k)$ within shell $51 \leqslant k \leqslant 55$ (curve K of figure 7).

scale separation, the implication is that differential large-scale distortion and advection on small scales maintains some level of dynamical dependence of small-scale evolution on large-scale structure in the infinite Reynolds number limit.

10. Competition with energy-cascading interactions, and apparent return to isotropy

From the analyses in the previous section, it is clear that in this numerical experiment the Fourier view of distant triadic interactions between forced large-scale modes and small-scale dynamics is described in physical space by differential advection, distortion and realignment of small-scale vorticity by the large-scale velocity field. These long-range dynamical processes compete with local and non-local interactions among motions not too widely separated in scale which, as discussed by Brasseur & Wei (1994), tend to move progressively smaller scales towards an isotropic state. As discussed in §3.4, the extent to which the anisotropizing influences of the long-range interactions successfully compete with the more local isotropizing influences depends on several interacting factors, including the separation between the large and small scales, the degree and structure of anisotropy at the large scales, the temporal evolution of large-scale structure, and time.

Because the timescale associated with distant interactions is smaller than the timescale of energy-cascading local interactions, we predicted in §3.4 that the small-scale anisotropy would initially increase, but then decrease as a new energy cascade is established between the forced large scales and the smallest scales. Furthermore, because the isotropizing influence of the cascade travels from the large to the small scales, we anticipated that the peak in the small-scale anisotropy would occur at later times within smaller scales. Both of these predictions were confirmed in figure 7(*a*), where the anisotropy in $E_{ij}(k)$ is plotted against time within different spectral shells. At small scales, anisotropy in $E_{ij}(k)$ increased then decreased with time, reaching a peak which is at later time in higher-wavenumber shells.

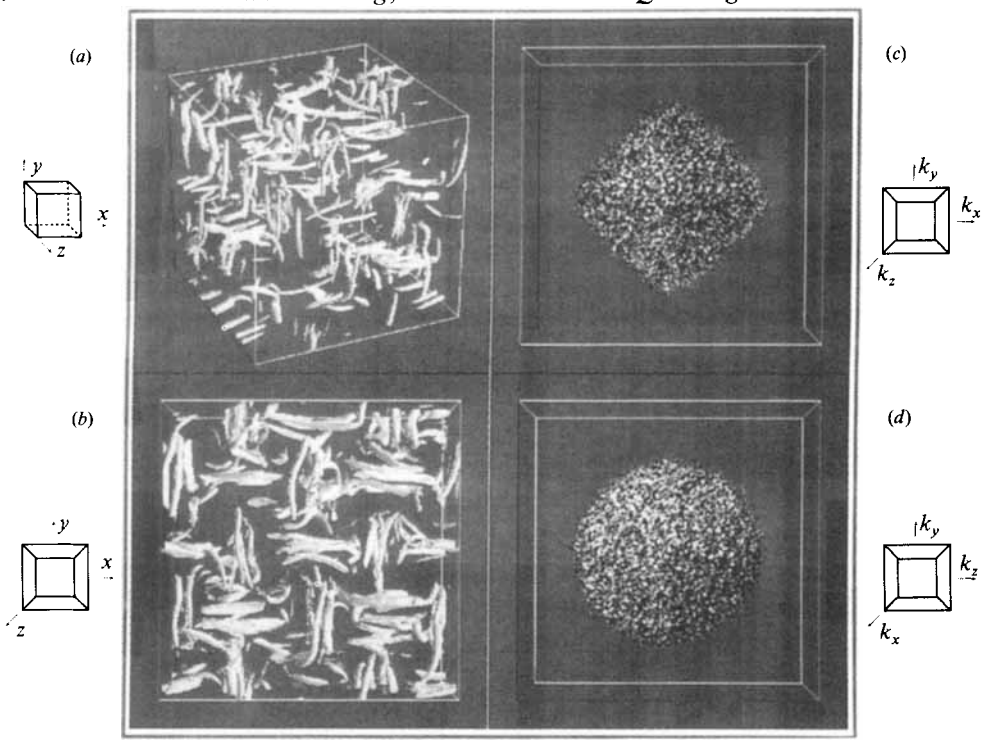

FIGURE 27. Three-dimensional isosurfaces of the small-scale enstrophy in physical space and in Fourier space at $t^* = 3.83$, a time when anisotropy in $E_{ij}(k)$ has vanished. (*a*), (*b*) The small-scale enstrophy in physical space from the same positions and with the same relative isosurface levels as figures 19 and 18(*d*). The vorticity vector field has been wavelet filtered with the spherically symmetric three-dimensional Mexican-hat wavelet with the peak in the filter at $k_a = 40$. Note that whereas the physical-space enstrophy structures have developed a spanwise orientation not existing in figures 18(*d*) and 19, much of the forced orientation apparent in figures 18(*d*) and 19 is also apparent here. (*c*), (*d*) The same relative isosurface of $\hat{\omega}_i(\boldsymbol{k})\,\hat{\omega}_i^*(\boldsymbol{k})$ from the same views as in figure 9. Note that whereas the isosurfaces are more spherically symmetric than in figure 9, particularly in (*d*), anisotropy in the enstrophy distribution is apparent in (*c*).

It was surprising, however, to discover in figure 7 that in all high-wavenumber shells, small-scale anisotropy in $E_{ij}(k)$ returned to zero for $t^* \gtrsim 3.5$ even with the continued existence of significant large-scale anisotropy in the forced modes (shell A). We had anticipated that anisotropy would decrease, perhaps to small values, but that a detectable level of anisotropy would remain at the small scales due to distant interactions with large scales which still contain significant levels of anisotropy. We show in this section that, whereas the influence of the distant triadic group relative to all other triadic interactions weakens considerably and small-scale anisotropy is significantly reduced, it does not vanish as suggested by figure 7. In reality, the small scales retain an anisotropic structure beyond $t^* = 3.5$ which is not detectable by the second moment; *higher-order moments are required to capture anisotropy statistically.*

Equation (8) indicates that the rate of intermodal energy exchange among small-scale modes due to distant triadic interactions relative to local triadic interactions is proportional to $[E(k_{LS})/E(k_{SS})]^{1/2}$ for fixed high-wavenumber and low-wavenumber shells k_{SS} and k_{LS}, respectively (LS and SS denote large-scale and small-scale, respectively). We anticipate, therefore, that the development of small-scale anisotropy in the forced simulation is related indirectly to the energy in the forced modes relative to the energy at the small scales. In figure 26 we plot $E(k_F)/E(k = 58)$ against time,

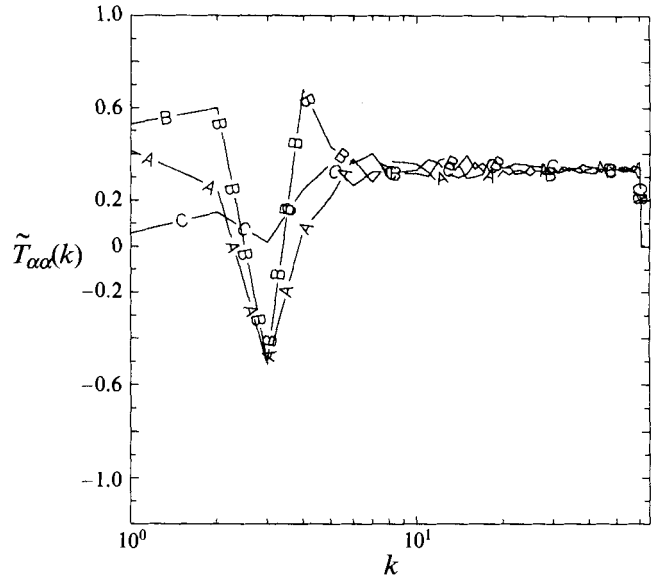

FIGURE 28. Diagonal components of the normalized radial energy transfer tensor $\tilde{T}_{\alpha\alpha}(k) = T_{\alpha\alpha}(k)/|T_{nn}(k)|$, at time $t^* = 3.830$ when $E_{ij}(k)$ is isotropic. Curves A, B, and C represent the $\alpha = 1, 2, 3$ diagonal components, respectively.

where $E(k_F)$ and $E(k = 58)$ are the energies in shells of unit width surrounding the forced modes and $k = 58$, respectively. Superimposed on the figure is the anisotropy of $E_{ij}(k)$ within shell K on figure 7 ($51 \leqslant k \leqslant 55$). Note that the anisotropy develops in the smallest scales when the energy within the forced modes relative to the small-scale modes is sufficiently large that anisotropic redistribution of small-scale energy by long-range interactions dominates the local group. Similarly, the apparent return to isotopy coincides with an increase in small-scale energy from the establishment of energy transfer from the forced modes to the small scales and consequent reduction in relative energy between large and small scales. We conclude, therefore, that as indicated by (8), the relative influence of the distant triadic group is stronger when the relative energy of large to small scales is larger. This observation supports the conclusion, for example, that in stationary turbulence deviations from local isotropy should be sought (*a*) at the smallest dissipative scales, where $E(k_{LS})/E(k_{SS})$ becomes asymptotically large, and (*b*) for increasing levels of large-scale anisotropy (Brasseur & Wei 1994).

The observation that energy at the large scales relative to small scales decreases when $t^* \gtrsim 2$ (figure 26) together with the decreasing level of large-scale anisotropy (figure 7*a*) is consistent with the observed reduction in small-scale anisotropy. Nevertheless, given that the initial state was isotropic by construction, we anticipate an observable, albeit significantly reduced, level of small-scale anisotropy beyond $t^* = 3.5$ in figure 7(*a*), given the significant level of large-scale anisotropy. This is indeed the case, as shown in figure 27 which shows the structure of the small-scale enstrophy field in Fourier space (figure 27*c*, *d*) and physical space (figure 27*a*, *b*) at $t^* = 3.83$, a time when anisotropy in $E_{ij}(k)$ has vanished. Figure 27(*c*, *d*) shows the same relative isosurface of $\hat{\omega}_i(\boldsymbol{k})\hat{\omega}_i^*(\boldsymbol{k})$ from the same views as in figure 9 at peak small-scale anisotropy. Note that whereas the isosurfaces in figure 27(*c*, *d*) are more spherically symmetric than in figure 9, particularly in the (k_y, k_z)-plane (figure 27*d*), anisotropy in enstrophy (or energy) distribution remains in the (k_x, k_y)-plane is apparent (figure 27*c*).

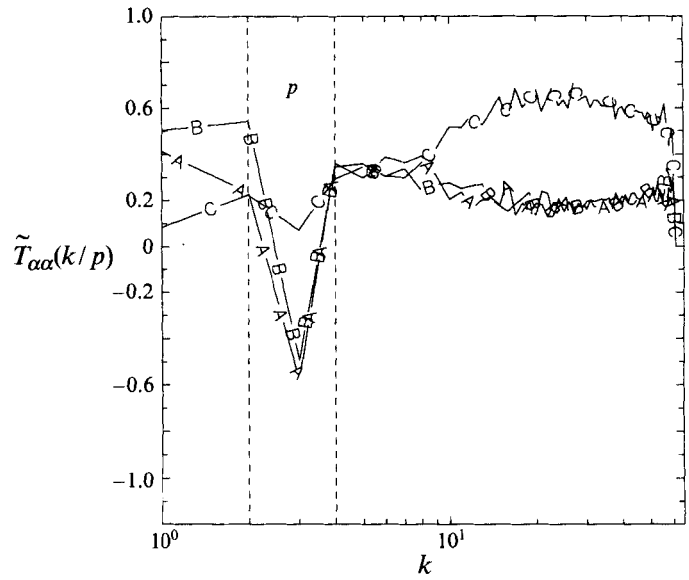

FIGURE 29. Diagonal components of the normalized radial energy transfer tensor limited to triads with one leg in shell $\tilde{T}_{\alpha\alpha}(k|p) = T_{\alpha\alpha}(k|p)/|T_{nn}(k|p)|$, at time $t^* = 3.830$ (when $E_{ij}(k)$ is isotropic) for $2 \leqslant p < 4$. Curves A, B, and C represent the $\alpha = 1, 2, 3$ diagonal components, respectively.

Corresponding small-scale enstrophy contours in physical space are shown in figure 27(*a*, *b*). Like figure 18(*d*), the vorticity vector field has been wavelet filtered with the spherically symmetric 3D Mexican-hat wavelet, as described in §§4 and 8, with the peak in the filter at $k_a = 40$. Figure 27(*a*, *b*) at $t^* = 3.83$ is shown from the same positions as figures 18(*d*) and 19 at peak anisotropy ($t^* = 1.915$) and has the same relative isosurface level. Note in comparing these figures that whereas the physical-space ensotrophy structures in figure 27(*a*, *b*) have developed a spanwise orientation not existing in figures 18(*d*) and 19, much of the forced orientation apparent in figures 18(*d*) and 19 is also apparent in figure 27(*a*, *b*). It is clear that the structure at $t^* = 3.83$ is very different from the initial isotropic state shown in figure 18(*a*) and that the long-range interactions continue to affect the small-scale structure during the period when $E_{ij}(k)$ contains no apparent anisotropy.

To understand how it is that $E_{ij}(k)$ can be isotropic while the non-local-to-distant energy transfer processes are anisotropic, consider figures 28–30 together with the dynamic equation for $E_{ij}(k)$ given by (24) integrated over spheres of radius k. Clearly from (24), if $E_{ij}(k)$ and $\partial E_{ij}(k)/\partial t$ are isotropic, as is the case in the small scales at $t^* = 3.83$, the radial energy transfer tensor $T_{ij}(k)$ must also be isotropic. This is the case, as shown in figure 28 where the diagonal components of the normalized transfer spectrum,

$$\tilde{T}_{ij}(k) \equiv \frac{T_{ij}(k)}{|T_{nn}(k)|}, \tag{41}$$

are plotted against k at $t^* = 3.83$. Absolute values are taken in the denominator to avoid confusion from the sign change in $T_{nn}(k)$ within the forced shell. Using the decomposition given in (26), $T_{ij}(k)$ may be written

$$T_{ij}(k) = \sum_p T_{ij}(k|p), \tag{42}$$

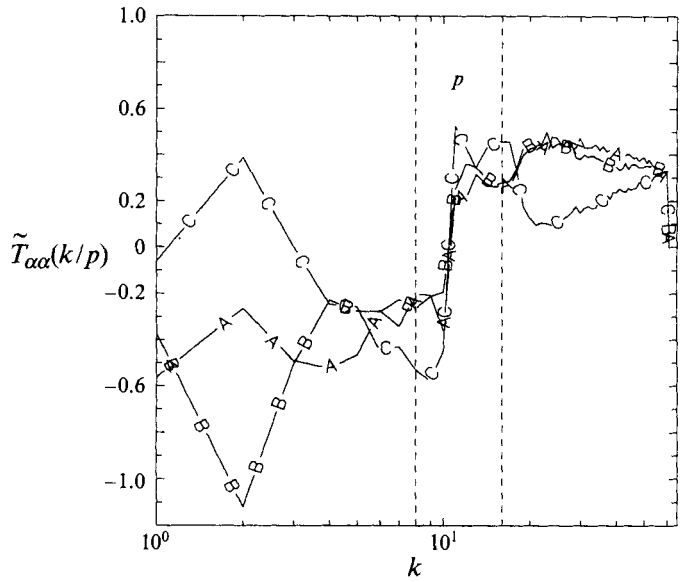

FIGURE 30. Diagonal components of $\tilde{T}_{\alpha\alpha}(k\,|\,p)$ as in figure 29 at time $t^* = 3.830$ for $8 \leqslant p < 16$. Curves A, B, and C represent the $\alpha = 1, 2, 3$ diagonal components, respectively.

where $T_{ij}(k\,|\,p)$ is the energy transfer to shell k due only to triadic interactions with one leg in shell p. The sum is over all p-shells covering the spectrum. Because the left-hand side of (42) is isotropic for high k, so must be the sum on the right-hand side. However, the individual terms in the sum on the right-hand side are not isotropic, as shown in figures 29 and 30.

Figure 29 shows the anisotropy in the energy transfer $T_{ij}(k\,|\,p)$ to velocity components u, v and w at the small scales (high k) due to triadic interactions with the shell $2 \leqslant p < 4$ containing the forced modes at $t^* = 3{,}83$, where

$$\tilde{T}_{ij}(k\,|\,p) \equiv \frac{T_{ij}(k\,|\,p)}{|T_{nn}(k\,|\,p)|}. \tag{43}$$

The figure is similar to figure 15 in YB and is consistent with the discussions in §3.3 where it is argued that the distant triadic interactions with the forced modes will transfer energy into the z-component of energy at the expense of the x- and y-energy components. Figure 29 shows this effect within the non-local to marginally distant triadic interactions in the simulation, at a time when $E_{ij}(k)$ is isotropic. Because energy transfer within the marginally distant group is non-isotropic, so must be the more local interactions, as shown in figure 30 with the p-shell now covering wavenumbers 8 to 16. Note that the energy transfer at the small scales within the more local group of triadic interactions is opposite to the marginally distant group with the forced modes; energy is distributed into the x- and y-energy components at the expense of the z-component. The anisotropic local-to-non-local triadic interactions act to counteract the anisotropic distant interactions so that the energy transfer tensor $T_{ij}(k)$ is isotropic. However, as discussed in §7, the anisotropic structure observed at the small scales follows from the marginally distant group, not the more local triadic interactions.

Whereas the second-order velocity moment and transfer spectra tensors are isotropic, the turbulence is not. The reason the second-order tensors do not detect the anisotropy in the signal is apparently the particular form of symmetry which exists in

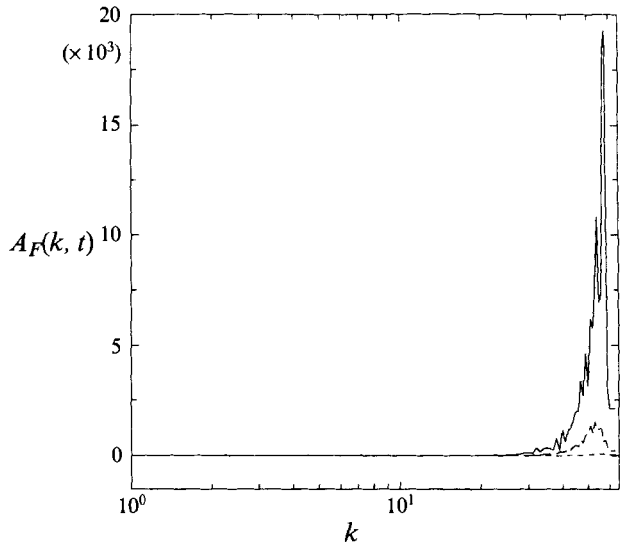

FIGURE 31. The normalized radial third-moment tensor, defined in (44) and (45) as a function of wavenumbers at the initial isotropic state, $t^* = 0$ (----); at peak anisotropy $t^* = 1.915$ (——); and when $E_{ij}(k)$ is isotropic $t^* = 3.830$ (——). $A_F = 0$ for isotropic turbulence as is clear from the initial state. Note by comparing this figure with figure 6 that the anisotropy of the radial energy tensor is sensitive to the anisotropic structure of the forced scales at $t^* = 3.83$ but not to the anisotropic structure of the small scales (curve J), whereas $A_F(k)$ is sensitive to small-scale anisotropy but not to the anisotropy in the forced scales.

the anisotropic turbulence structure. Compare figure 9(a, b) at peak anisotropy in $E_{ij}(k)$ with figure 27(c, d) where $E_{ij}(k)$ is isotropic. In both sets of figures the energy distribution has a symmetry in the (k_x, k_y)-plane such that any mutually perpendicular pair of axes sees the same energy or enstrophy distribution at high wavenumbers. The same statement can be made about the (k_y, k_z)-plane in figure 27(d), but not at peak anisotropy in figure 9(b). We speculate, therefore, that $E_{ij}(k)$ reflects primarily the non-spherical symmetry in the (k_y, k_z)-plane, and that the evolution of $\mathrm{III}_A(k)$ at high k in figure 7 is a reflection of the distortion of the energy distribution in the (k_y, k_z)-plane, first from a spherical distribution in figure 1 to an elliptical distribution in figure 9 (t^* from 0 to 2), then from the elliptical energy distribution back to a spherical distribution in figure 27(d) (t^* from 2 to 3.5).

Because the second moment appears incapable of statistically detecting the anisotropic structure at the small scales in the forced simulation when $t^* \gtrsim 3.5$, it appears that higher-order moments are needed to quantify small-scale anisotropy, a reminder of Kolmogorov's (1941) original argument in which local isotropy is defined in terms of probability distribution functions whose complete specification requires knowledge of statistical moments of all orders. To test this hypothesis with the current simulation, we calculated the Fourier transform of the third moment, $F_{ijl}(\boldsymbol{r}) \equiv \langle v_i(\boldsymbol{x}) v_j(\boldsymbol{x}+\boldsymbol{r}) v_l(\boldsymbol{x}) \rangle$, $F_{ijl}(\boldsymbol{k})$. From Monin & Yaglom (1975, pp. 63, 70)

$$F_{ijl}(\boldsymbol{k}) = u_l^*(\boldsymbol{k}) \sum_{\boldsymbol{p}} u_i(\boldsymbol{p})\, u_j(\boldsymbol{k}-\boldsymbol{p}) + \text{c.c.}, \tag{44}$$

where the complex conjugate c.c. is added to make the tensor real-valued. It may be shown that when integrated over a sphere of radius k, $F_{ijl}(k)$ is zero if the scales within

the shell k are statistically isotropic. In figure 31 we plot $A_F(k)$ against k, where $A_F(k)$ is the square of $F_{ijl}(k)$ normalized with the energy within the shell k:

$$A_F(k) = \frac{F_{ijl}(k)\,F_{ijl}(k)}{[E_{nn}(k)]^3}. \tag{45}$$

In figure 31 $A_F(k)$ is plotted at the initial isotropic state ($t^* = 0$), at peak anisotropy in $E_{ij}(k)$ ($t^* = 1.915$), and when the anisotropy in $E_{ij}(k)$ has disappeared ($t^* = 3.83$). At the initial isotropic state $A_F(k)$ is zero for all k. At both $t^* = 1.915$ and 3.83, however, $A_F(k)$ departs from zero at the small scales, with the lower small-scale anisotropy at $t^* = 3.83$ rather than at $t^* = 1.915$.†

Note by comparing figure 31 with figure 6 that the anisotropy of the radial energy tensor is sensitive to the anisotropic structure of the forced scales at $t^* = 3.83$ but not to the anisotropic structure of the small scales (curve J), whereas $A_F(k)$ is sensitive to small-scale anisotropy but not to the anisotropy in the forced scales! We conclude, therefore, that different statistical measures are sensitive to different anisotropic structure. Furthermore, whereas the deviation from anisotropy in a given statistical measure does imply the existence of anisotropic structure in the turbulence, *a null result in a single statistical measure of anisotropy does not necessarily imply that the statistical structure of the turbulence is isotropic.*

11. Discussion: the potential for deviations from local isotropy

In general terms, this study demonstrates the influence of long-range interactions which are present, in principle, in the high Reynolds number limit. We show that the small-scale dynamics associated with the more long-range interactions in the numerical experiment follow a three-dimensional temporal evolution which is predictable in many important respects from the asymptotic form of Navier–Stokes nonlinearity applicable in the infinite Reynolds number limit. Combined with earlier studies by Brasseur (1991), Yeung & Brasseur (1991) and Brasseur & Wei (1994), the study implies the existence of a direct influence of large-scale evolution on small-scale dynamics which is always present in principle, but which may be strongly stimulated during non-equilibrium transients in large-scale energy and structure.

The study focuses on the relationship between the spectral view and the physical-space view in the evolution of the small scales due to long-range interactions. We find that in this numerical experiment the long-range interactions are a reflection of differential advection and distortion of small-scale vortical elements by the large-scale energy field. It appears that the large scales have the ability to redistribute the small-scale motions without directly giving up energy to these motions. The degree of small-scale restructuring depends on the energy and timescales of coherence in the large-scale structure, and on the transients in large-scale restructuring.

It is difficult to extract dynamical details of interactions among scales within the physical-space view. For this reason, detailed dynamical analysis of scale interactions is best carried out within a decomposition explicitly focusing on scale. We use the Fourier representation as a useful decomposition in scale, where our focus is on the three-dimensional structure of Fourier decomposition. Fourier decomposition is natural in homogeneous turbulence in that the three-dimensional distribution of Fourier modes provides an elemental description of scale that includes direction,

† The reduction in $A_F(k)$ at the highest k is apparently due to dealiasing and numerical error in spectral regions where energy levels are very low.

energy and phase information while at the same time providing a readily interpretable set of dynamical equations, which we exploited in this work. Because a Fourier mode collects information from many ensembles of structures within the turbulent flow, when the turbulence structure is independent of position, the Fourier mode represents the net contribution to a given harmonic scale in a given direction. (The non-locality of Fourier is advantageous for scale decomposition of statistically homogeneous turbulence in that each Fourier mode samples all statistically similar structural elements within the signal.) Nevertheless, the main issue is not so much the decomposition itself, but rather the relationship between the three-dimensional time-evolving structure within the decomposition and the three-dimensional time-evolving structure of the signal. We take the position in this paper that once this relationship is clearly understood, the dynamics in Fourier space may be interpreted in terms of structural dynamics.

Brasseur & Wei (1994) argued that, whereas local and non-local scale interactions are forward cascading on average, distant interactions tend to redistribute energy within spectral shells. As a consequence, distant interactions from a non-isotropic large-scale energy distribution lead to depletions of energy in high-wavenumber regions of Fourier space which, in the current numerical experiment correspond to the directions of the four low-wavenumber forced modes and the direction perpendicular to the four forced modes. The result, we have shown, is the concentration of high-wavenumber spectral energy and vorticity along four coordinate directions, consistent with the distant triadic equations and the arguments of Brasseur & Wei (1994). As importantly, we have observed a certain *locality in Fourier space*. In physical space, a large-scale field of counter-rotating vortices is established which advects small-scale vorticity into stagnation-point regions, distorting the vortex tubes so as to align with the principal strain directions. The result is a collection of small-scale vortices aligned with the x- and y-axes. In Fourier space these small-scale vortices are described within localized groups of Fourier modes surrounding the k_x- and k_y-axes. We showed that the dynamical influence of long-range interactions at the small scales is to redistribute vorticity and energy at high wavenumbers in Fourier space as a reflection of a redistribution of vorticity and energy at the small scales in physical space. This redistribution is such that local regions in Fourier space correspond precisely to spatially localized, vortical structures in physical space. Even more interesting is that the Fourier modes surrounding the k_x- and k_y-axes separately describe subsets of vortices in physical space aligned with the x- and y-directions, respectively. That is, the dynamical evolution and structure of local regions in Fourier space correspond precisely to the dynamical evolution and structure of subsets of pervasively distributed, but spatially localized, vortical structures in physical space.

Structure in physical space is described by the distribution of both energy and phase in Fourier space. Uniform distributions of energy and phase of Fourier modes on spheres centred on the origin in three-dimensional Fourier space are necessary for a statistically isotropic structure to exist in physical space at the scale of the spheres in homogeneous turbulence. Showing a non-isotropic distribution in either is sufficient to argue for anisotropy. We have made extensive use in this study of non-isotropic distributions of energy on spheres implying the existence of anisotropy at those scales. However, additional study of the distant triadic equations indicates that redistribution of energy tends to be a partner with redistribution of phase at the small scales within the distant triadic group. In particular, we have found that those Fourier modes within the local regions of high-wavenumber Fourier space directly associated with subsets of small-scale vortices in physical space are phase-coupled, and that the phase coupling,

like the redistribution of energy itself, is a direct consequence of the long-range interactions in the simulation. The implication is that structure in the physical-space view, localized but pervasively spread throughout the turbulence, is associated with spectrally local concentrations of dynamically coupled Fourier modes. More recent work has shown that the same statement can be made in naturally decaying turbulence (Brasseur & Wang 1993).

The work of Brasseur & Wei (1994) suggests that local-to-non-local cascading interactions have an isotropizing influence at the small scales. We showed here that the timescale for distant interactions is shorter than for local interactions, so that the initial anisotropizing influence of distant interactions should be reduced by local-to-non-local interactions once large-scale energy has cascaded to the small scales. Consistent with this argument, we found in the current study that long-range-induced small-scale anisotropy reached a peak before diminishing once again upon arrival of forward-cascading large-scale energy. However, analysis of the local-to-non-local triadic interactions which contribute to the energy-transfer spectral tensor indicates that the isotropizing influences of the energy-cascading interactions are somewhat more complex than the description give by Brasseur & Wei (1994) in that the more non-local cascading interactions appear to transfer energy anisotropically, but in a manner opposing the anisotropic structure induced by the marginally distant interactions. Further study is needed to clarify these observations.

At this point we should explicitly address a question that was brought out in the course of the review – is it possible that the development of small-scale anisotropy from $t^* = 0$ to 1.915 (shown, for example, in figure 7) is a consequence of a cascading series of instabilities that transfer information from the forced scales to the small scales? There are many reasons, discussed at length in §§6–10, why this cascade-based model cannot explain the results of the simulation. Most obvious among these is that the large-scale forced modes do not become unstable during the period of anisotropy development, as is clear visually in figure 18(*c*). Indeed, figure 7 indicates that the period over which the small scales develop a well-defined anisotropic structure ($0 \leqslant t^* \leqslant 1.915$) is also the period where the two-dimensional large-scale forced vortices form (this concurrent development of large- and small-scale structure is especially clear in animations we created of large- and small-scale enstrophy isosurfaces). Viewed spectrally, a cascade-based explanation would require that the smallest scales ($k \sim 50$, say, quantified in figures 6, 7, 10, 13–17) are formed from triadic interactions with scale separations primarily in the range 2–7 (Zhou 1993*a*, *b*; Brasseur & Wei 1994). That is, spectral wavenumbers $k \sim 7$–25 would be primarily responsible for the development of anisotropic structure within scales $k \sim 50$. However, as shown in figure 7, the development of anisotropy in the smaller scales ($k \sim 50$) precedes the development of anisotropy in the larger scales ($k \sim 7$–25). Indeed, the observation that the development of small-scale anisotropy proceeds from the smallest scales to larger scales (figure 7*b*) cannot be explained with cascade-based arguments and is the first of many results which can only be explained from the asymptotic form of the triad equations in the distant limit (§§3, 7). As discussed in §10, however, the reduction in anisotropy when $t^* > 1.915$ *is* a consequence of cascading energy.

A general conclusion of this work is that two competing dynamics interact within the simulated turbulent flow: (i) direct transfer of large-scale structural information (without direct energy transfer) from the large-scale forced modes, first to the smallest turbulent scales then progressively to larger turbulent scales, and (ii) transfer of energy (along with structural modification) from the large forced scales to smaller scales, eventually reaching the smallest scales of motion. Detailed analysis in this paper and

YB has shown the first dynamics to be a consequence of long-range scale interactions which force a redistribution of energy and phase at the small scales in a manner directly related to the distribution of energy and phase within the large forced scales. The second dynamics is from 'local-to-non-local' energy-cascading triadic interactions which transfer energy and phase information from larger to somewhat smaller scales, but in a manner which weakens the anisotropizing influence of the long-range interactions at progressively smaller scales. Consequently, the peaks in the anisotropy curves of figure 7 move from larger to smaller scales with time.

We should also mention a recently completed study by Zhou, Yeung & Brasseur (1994) which explicitly addresses the argument of complete cancellation within the distant triadic group by Waleffe (1992). The Zhou *et al.* study further confirms the conclusions from this work – that complete cancellation within long-range interactions does not take place and that the long-range interactions are responsible for the development and maintenance of small-scale anisotropy during large-scale forcing. The study also shows explicitly that, while direct energy transfer from the large-scale forced structure to smaller scales decreases rapidly with scale separation, the anisotropic restructuring of the small scales increases with scale separation, confirming the triad-based conclusions in this study.

Although it appears from the second moment that the small scales return to an isotropic state, we show that in reality they do not. This observation is important for experimental searches for deviations from local isotropy which, of necessity, can only use limited statistical measures of small-scale anisotropy. In the current study the deviatoric part of the second moment velocity–velocity correlation tensor is used as a measure of local anisotropy. We learned in this study that the second-moment velocity tensor is sensitive to some anisotropic characteristics, but insensitive to others. Once the energy cascade re-establishes itself after forcing, the second moment becomes insensitive to the particular small-scale anisotropic structure which exists at the later times. Nevertheless, the three-dimensional distribution of small-scale spectral energy shows clearly that significant small-scale anisotropy remains at later times. The third velocity moment, on the other hand, *is* able to statistically detect small-scale anisotropy, but is insensitive to large-scale anisotropy, at these later times. We conclude, therefore, that whereas anisotropy in the measure implies anisotropy in the signal, the converse is not necessarily true. A null result in a single statistical measure of anisotropy is a necessary condition, but is not sufficient to guarantee isotropy. Some care must be taken, therefore, in the use of limited anisotropy measures in analysing local isotropy at the small scales.

This work indicates that Fourier modes, and their corresponding scales of motion, are dynamically coupled over large separations in scale, the strength of the coupling increasing with the relative energies of the large- and small-scale modes. Within individual triads, then, the strongest couplings tend to be between the large energy-containing scales and the dissipative scales with local Reynolds number of order one or greater. Because an element of small-scale evolution is coupled to the structure and evolution of the large scales within the distant triadic group, if the large scales have a statistically preferred direction, the energy transfer within the distant group of triadic interactions also has a preferred direction. This directional dependence persists in ensemble averages of statistically similar flows. The distant group, then, is in principle at variance with the Kolmogorov hypothesis of statistical large–small scale independence in the asymptotic limit. However, the deviation from local isotropy is a matter of degree that depends on a variety of interacting factors (Brasseur & Wei 1994). If the Kolmogorov hypothesis is viewed as an approximation of reality, then in practice

the approximation may be a very good one in many instances. By the same token, however, if one is aware of the existence of long-range dynamical processes which are at variance with the hypothesis, and if one understands the structure and consequences of those dynamical processes, then the potential exists to identify situations where the hypothesis breaks down. This paper has provided some understanding of when and why the hypothesis breaks down. It appears that non-equilibrium turbulent flows are particularly susceptible to the effects of long-range interactions and that turbulence closures applied to strongly non-stationary and non-equilibrium flows may need to include these effects to properly capture the temporal variations in turbulence evolution.

We acknowledge valuable interactions in the course of this work with K. R. Sreenivasan, Lex Smits, Jim McMichael and Pat Purtell. Many interesting discussions were had surrounding various elements of this work with Andzrej Domaradzki, Ye Zhou, John Lumley, Julian Hunt, Christos Vassilicos, Mark Nelkin, John Kim, Bob Antonia, Seyed Saddoughi and Peter Bradshaw. The interactions with the referees led to a major revision of this paper so as to make clear, we hope, the important messages resulting from the study. We value all our discussions with our colleagues and hope they continue. We gratefully acknowledge support from grants AFOSR 89-0026 and URI/AFOSR 90-0113. The computational resources for this work were made available from the Cornell Theory Center (CNSF), which receives major funding from the National Science Foundation, New York State Science and Technology Foundation and the Corporate Research Institute.

REFERENCES

ANTONIA, R. A., ANSELMET, F. & CHAMBERS, A. J. 1986 Assessment of local isotropy using measurements in a turbulent plane jet. *J. Fluid Mech.* **163**, 365–391.

BATCHELOR, G. K. 1953 *The Theory of Homogeneous Turbulence.* Cambridge University Press.

BRASSEUR, J. G. 1991 Comments on the Kolmogorov hypothesis of isotropy in the small scales. *AIAA Paper* 91-0230.

BRASSEUR, J. G. & CORRSIN, S. 1987 Spectral evolution of the Navier–Stokes equations for low order couplings of Fourier modes. In *Advances in Turbulence* (ed. G. Comte-Bellot & J. Mathieu), pp. 152–162. Springer.

BRASSEUR, J. G. & WANG, Q. 1992 Structural evolution of homogeneous turbulence at different scales analyzed using 3D wavelet transforms. *Phys. Fluids* A **4**, 2538–2554.

BRASSEUR, J. G. & WANG, Q. 1993 Locality in Fourier space, locality in physical space and the relationship between the two. *Bull. Am. Phys. Soc.* **38**, 2228 (1993 meeting of the Division of Fluid Dynamics of the American Physical Society, Albuquerque, New Mexico).

BRASSEUR, J. G. & WEI, C.-H. 1994 Interscale dynamics and local isotropy in high Reynolds number turbulence within triadic interactions. *Phys. Fluids* **6**, 842–870.

BRASSEUR, J. G. & YEUNG, P. K. 1991 Large and small-scale coupling in homogeneous turbulence: analysis of the Navier–Stokes equation in the asymptotic limit. *Proc. Eighth Symposium on Turbulent Shear Flows, Munich, Germany*, pp. 16-4-1–16-4-6.

BROWNE, L. W. B., ANTONIA, R. A. & SHAH, D. A. 1987 Turbulent energy dissipation in a wake. *J. Fluid Mech.* **179**, 307–326.

CHAMPAGNE, F. H. 1978 The fine-scale structure of turbulence velocity field. *J. Fluid Mech.* **86**, 67–108.

COMBES, J. M., GROSSMANN, A. & TCHAMITCHIAN, P. (eds.) 1989 *Wavelets.* Springer.

DOMARADZKI, J. A. & ROGALLO, R. S. 1990 Local energy transfer and nonlocal interactions in homogeneous, isotropic turbulence. *Phys. Fluids* A **2**, 413–426.

DURBIN, P. A. & SPEZIALE, C. G. 1991 Local anisotropy in strained turbulence at high Reynolds numbers. *Trans. ASME* I: *J. Fluids Engng* **113**, 707–709.

GEORGE, W. K. & HUSSEIN, H. J. 1991 Locally axisymmetric turbulence. *J. Fluid Mech.* **233**, 1–23.

JIMENEZ, J., WRAY, A., SAFFMAN, P. G. & ROGALLO, R. S. 1993 The structure of intense vorticity in homogeneous isotropic turbulence. *J. Fluid Mech.* **255**, 65–90.

KIM, J. & ANTONIA, R. A. 1993 Isotropy of the small scales of turbulence at low Reynolds numbers. *J. Fluid Mech.* **251**, 219–238.

KOLMOGOROV, A. N. 1941 The local structure of turbulence in incompressible viscous fluids for very large Reynolds numbers. *C.R. Acad. Sci. URSS* **30**, 301–305.

KARYAKIN, M. Y., KUZNETZOV, V. R. & PRASKOVSKY, A. A. 1991 *Izv. Adad. Nauk SSSR, Mech. Zhidk. i Gaza* **5**, 51–59.

LIN, W.-Q. 1993 Structural and dynamical characteristics of intermittent structures in homogeneous turbulent shear flow. PhD thesis, Department of Mechanical Engineering, Pennsylvania State University, University Park, PA.

LUMLEY, J. L. 1992 Some comments on turbulence. *Phys. Fluids* A **4**, 203–212.

LUMLEY, J. L. & NEWMAN, G. R. 1977 The return to isotropy of homogeneous turbulence. *J. Fluid Mech.* **82**, 161–178.

MELANDER, M. V., MCWILLIAMS, J. C. & ZABUSKY, N. J. 1987 Axisymmetrization and vorticity-gradient intensification of an isolated two-dimensional vortex through filamentation. *J. Fluid Mech.* **178**, 137–159.

MESTAYER, P. 1982 Local isotropy and anisotropy in a high-Reynolds-number turbulent boundary layer. *J. Fluid Mech.* **125**, 475–503.

MONIN, A. S. & YAGLOM, A. M. 1975 *Statistical Fluid Mechanics: Mechanics of Turbulence*, vol. 2, MIT Press.

NELKIN, M. 1993 Pressure fluctuations and local isotropy in high Reynolds number turbulence. In *Unstable and Turbulent Motion of Fluid* (ed. S. Kida), pp. 156–161. World Scientific.

ONSAGER, L. 1949 Statistical hydrodynamics. *Nuovo Cim.* Suppl. 6 (2), 279.

POLIFKE, W. & SHTILMAN, L. 1989 The dynamics of helical decaying turbulence. *Phys. Fluids* A **1**, 2025–2033.

ROGALLO, R. S. 1981 Numerical experiments in homogeneous turbulence. *Tech. Mem.* 81315. NASA Ames Research Center.

SADDOUGHI, S. G. & VEERAVALLI, S. V. 1994 Local isotropy in high Reynolds number turbulent shear flows. *J. Fluid Mech.* **268**, 333–372.

SHE, Z.-S., JACKSON, E. & ORSZAG, S. A. 1988 Scale-dependent intermittency and coherence in turbulence. *J. Sci. Comput.* **3**, 407–434.

SHE, Z.-S., JACKSON, E. & ORSZAG, S. A. 1990 Intermittent vortex structures in homogeneous isotropic turbulence. *Nature* **344**, 226–228.

SREENIVASAN, K. R. 1991 On local isotropy of passive scalars in turbulent shear flows. *Proc. R. Soc. Lond.* A **434**, 165–182.

VAN ATTA, C. 1991 Local isotopy of the smallest scales of turbulent scalar and velocity fields. *Proc. R. Soc. Lond.* A **434**, 139–147.

VINCENT, A. & MENEGUZZI, M. 1991 The spatial structure and statistical properties of homogeneous turbulence. *J. Fluid Mech.* **225**, 1–20.

WALEFFE, F. 1992 The nature of triad interactions in homogeneous turbulence. *Phys. Fluids* A **4**, 350–363.

WANG, Q. & BRASSEUR, J. G. 1993 Application of nonsymmetrical 3D wavelet filters to the analysis of anisotropic turbulence data. In *ASME 1993 Forum on Turbulent Flows*, FED-Vol. 155, pp. 137–142.

WANG, Q., BRASSEUR, J. G., SMITH, R. W. & SMITS, A. J. 1994 Multi-dimensional continuous wavelet transforms and applications to turbulence data. *Proc. R. Soc. Lond.* A (submitted).

YEUNG, P. K. & BRASSEUR, J. G. 1991 The response of isotropic turbulence to isotropic and anisotropic forcing at the large scales. *Phys. Fluids* A **3**, 884–897 (referred to herein as YB).

YEUNG, P. K. & POPE, S. B. 1988 An algorithm for tracking fluid particles in numerical simulation of homogeneous turbulence. *J. Comput. Phys.* **79**, 373–416.

YEUNG, P. K. & POPE, S. B. 1989 Lagrangian statistics from direct numerical simulations of isotropic turbulence. *J. Fluid Mech.* **207**, 531–586.

ZHOU, Y. 1993*a* Degrees of locality of energy transfer in the inertial range. *Phys. Fluids* A **5**, 1092–1094.

ZHOU, Y. 1993*b* Interacting scales and energy transfer in isotropic turbulence. *Phys. Fluids* A **5**, 2511–2524.

ZHOU, Y., YEUNG, P. K. & BRASSEUR, J. G. 1994 Scale disparity and spectral transfer in anisotropic numerical turbulence. *Phys. Fluids* (submitted).